BIOPHYSICS

Live-cell quantification reveals viscoelastic regulation of synapsin condensates by α-synuclein

Huan Wang[1], Christian Hoffmann[2], Johannes V. Tromm[2], Xiao Su[3,4], Jordan Elliott[1], Han Wang[2], Mengying Deng[1], Conor McClenaghan[5], Jean Baum[1], Zhiping P. Pang[3,4], Dragomir Milovanovic[2,6,7]*, Zheng Shi[1,8]*

Synapsin and α-synuclein represent a growing list of condensate-forming proteins where the material states of condensates are directly linked to cellular functions (e.g., neurotransmission) and pathology (e.g., neurodegeneration). However, quantifying condensate material properties in living systems has been a substantial challenge. Here, we develop micropipette aspiration and whole-cell patch-clamp (MAPAC), a platform that allows direct material quantification of condensates in live cells. We find 10,000-fold variations in the viscoelasticity of synapsin condensates, regulated by the partitioning of α-synuclein, a marker for synucleinopathies. Through in vitro reconstitutions, we identify multiple molecular factors that distinctly regulate the viscosity, interfacial tension, and maturation of synapsin condensates, confirming the cellular roles of α-synuclein. Overall, our study provides unprecedented quantitative insights into the material properties of neuronal condensates and reveals a crucial role of α-synuclein in regulating condensate viscoelasticity. Furthermore, we envision MAPAC applicable to study a broad range of condensates in vivo.

INTRODUCTION

Biomolecular condensates that form through phase separation have recently come to prominence as key contributors to various cellular functions (*1*, *2*). The viscoelasticity of condensates regulates the kinetics of biochemical reactions in the dense phase, whereas an aberrant increase in condensate viscoelasticity has been associated with neurodegenerative diseases (*3*–*8*). Beyond bulk viscoelasticity, there has been a growing interest in the interfacial properties of condensates (*9*), focusing on their roles in regulating the structure of multiphase condensates (*10*–*13*), the growth and size of condensates (*14*–*16*), and the interactions between condensates with other cellular components such as biopolymers (*15*, *17*–*20*) and membrane-bound organelles (*21*–*25*).

Neuronal communication critically relies on the regulated secretion of synaptic vesicles (SVs) at specialized sites termed synapses. The cluster of SVs at synaptic boutons represents a prominent example of biomolecular condensates (*23*, *26*, *27*), assembled by the highly abundant, intrinsically disordered synapsin family of proteins (*28*, *29*). Synapsin/SV condensates act as reaction centers that are able to recruit α-synuclein (*30*–*32*), a major synaptic protein implicated in the regulation of SV cycles and the pathology of neurodegenerative diseases collectively known as synucleinopathies (*33*). Genetic data suggest a tight balance of synapsin and α-synuclein concentrations that directly affects the mesoscale organization of SV clusters at synapses (*34*). The altered concentration of α-synuclein disrupts SV packing (*35*, *36*) and impairs neurotransmission (*31*, *33*, *34*, *37*). Therefore, the material properties of synapsin condensates and factors that regulate these properties can directly affect neuronal signaling and neurodegenerative diseases.

While previous data suggest that α-synuclein plays a role in the organization of synapsin/SV assemblies, direct measurements are lacking to determine whether and how α-synuclein regulates the material state of synapsin condensates due to technical limitations. Recently, we demonstrated that micropipette aspiration (MPA) can be applied to quantify the material properties of condensates in vitro (*38*, *39*). MPA is a label-free technique that simultaneously measures both the viscosity and interfacial tension of condensates (*38*, *40*). This differentiates MPA from widely used techniques such as fluorescence recovery after photobleaching (FRAP), fluorescence correlation spectroscopy (FCS), microrheology, and droplet fusion, where either only the viscosity or a ratio of viscosity to interfacial tension of condensates can be probed (*41*). Despite recent progress in which fluorescence-based techniques have been used in cells, quantification of condensate material properties in living systems remains a severe hurdle for understanding condensates in their native environment (*8*, *42*, *43*).

Here, we develop a correlative MPA and whole-cell patch-clamp (MAPAC) platform to study the material properties of synapsin condensates in living mammalian cells. Integration of these two techniques allows us to quantify the material properties of cellular condensates while monitoring cell health via membrane voltage (*44*). The viscous and elastic moduli of condensates vary by four orders of magnitude between cells, and these variations are directly correlated with the partitioning of α-synuclein and, to a lesser extent, the partitioning of synapsin into condensates.

To obtain a better mechanistic understanding of the cellular data, we explore the material properties of reconstituted synapsin

---

[1]Department of Chemistry and Chemical Biology, Rutgers University, Piscataway, NJ 08854, USA. [2]Laboratory of Molecular Neuroscience, German Center for Neurodegenerative Diseases (DZNE), Berlin 10117, Germany. [3]The Child Health Institute of New Jersey, Robert Wood Johnson Medical School, Rutgers University, New Brunswick, NJ 08901, USA. [4]Department of Neuroscience and Cell Biology, Robert Wood Johnson Medical School, Rutgers University, New Brunswick, NJ 08901, USA. [5]Center for Advanced Biotechnology and Medicine, and Departments of Pharmacology and Medicine, Robert Wood Johnson Medical School, Rutgers University, Piscataway, NJ 08854, USA. [6]Einstein Center for Neuroscience, Charité-Universitätsmedizin Berlin, Corporate Member of Freie Universität Berlin, Humboldt-Universität Berlin and Berlin Institute of Health, Berlin 10117, Germany. [7]German Center for Neurodegenerative Diseases (DZNE), Bonn 53127, Germany. [8]Cancer Pharmacology Research Program, Cancer Institute of New Jersey, Rutgers University, New Brunswick, NJ 08901, USA.

*Corresponding author. Email: zheng.shi@rutgers.edu (Z.S.); dragomir.milovanovic@dzne.de (D.M.)

condensates in vitro by varying synapsin domains and the condensate environment. We show that condensates formed by synapsin's intrinsically disordered region (IDR) alone have reduced viscosity. In contrast, α-synuclein and two additional factors (crowding agents and SVs) significantly increase the viscosity of synapsin condensates. However, these factors have distinct effects on the interfacial tension of synapsin condensates: The interfacial tension increases with polyethylene glycol (PEG) and decreases with SVs but remains unaltered with the partitioning of α-synuclein. Furthermore, we observe a marked maturation phenomenon in which the viscoelasticity of synapsin/α-synuclein condensates increases more than 1000-fold after a 20-hour incubation in whole cytosolic extract. Removing α-synuclein slows the maturation process, underscoring the importance of α-synuclein in regulating the material properties of synapsin condensates.

Together, our results provide unprecedented quantitative understanding of synapsin condensates, highlighting an effective cellular control of condensate viscoelasticity via compositional modulations. Moreover, we present MAPAC, a broadly applicable platform that allows intricate examinations of individual condensates in living cells.

RESULTS

MAPAC allows direct measurements of synapsin condensates in live cells

To probe condensates in live cells, an electrode-containing micropipette filled with intracellular buffer solution was positioned to break the plasma membrane near a condensate (Fig. 1A). Once the locally broken plasma membrane sealed to the edge of the pipette tip,

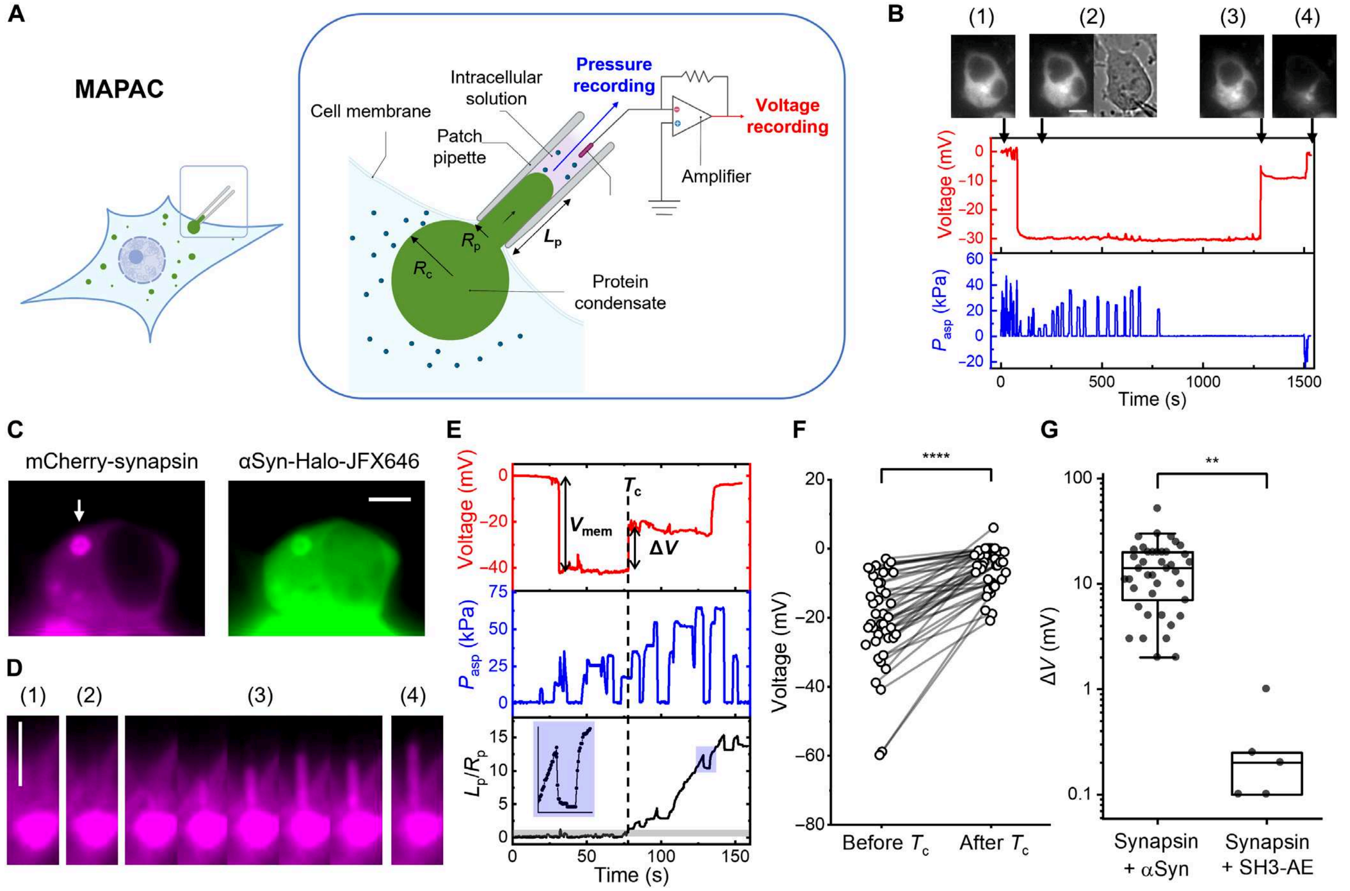

Fig. 1. Development of MAPAC for condensate measurements in live cells. (**A**) Schematic representation of the MAPAC platform. (**B**) Testing the effect of aspiration pressure (blue) on cell membrane voltage recording (red) on a human embryonic kidney (HEK) 293T cell expressing mCherry-synapsin and α-synuclein (αSyn)–BFP (blue fluorescent protein). Fluorescence images of synapsin correspond to time points before (1) and after (2) break-in and before (3) and after (4) losing membrane seal. A transmitted-light image is included for time point (2). The voltage jumped to 0 mV before time point (4) due to an intentional ejection pressure that broke the membrane seal, followed by significant leakage of cytosolic fluorescence. (**C**) Fluorescence images showing a HEK 293T cell co-expressing mCherry-synapsin (magenta) and αSyn–Halo (stained with JFX-646; green). The arrow represents the micropipette positioned next to a condensate. (**D**) Fluorescence images of the synapsin/α-synuclein condensate before (1) and after (2) micropipette break-in, during MAPAC (3), and after V_{mem} jumped to zero (4). (**E**) MAPAC recording of membrane voltage (red), aspiration pressure (blue), and normalized aspiration length (black) for the condensate in (D). The micropipette entrance of the condensate at T_c (dashed line) accompanied a voltage jump (ΔV). The gray shade represents $L_p/R_p < 1$. The blue shade is zoomed-in on the left. (**F**) Voltage recordings before and after a synapsin/α-synuclein condensate entered the tip of the micropipette. $n = 41$ cells. $****P < 10^{-4}$, paired t test. (**G**) ΔV measured on synapsin/α-synuclein condensates and synapsin/intersectin-SH3 condensates ($n = 5$). $**P < 10^{-2}$, Student's t test. Scale bars, 5 μm. In box plots, the central lines denote the median, the boxes span the interquartile range (25 to 75%), and the whiskers extend to 1.5 times the interquartile range, same below.

suction pressures were gently applied so that the nearby condensate could flow into the tip of the micropipette for subsequent quantifications. To ensure accurate measurement of condensate deformation, the micropipette was bent near the tip so that the aspiration of the condensate would happen within the imaging plane (fig. S1A). Meanwhile, the recorded membrane voltage served as a sensitive monitor for the stability of the intracellular environment during MAPAC.

First, we tested the effect of aspiration pressure (P_{asp}) on the stability of voltage recording. Under frequent pressure perturbations that resemble those used to probe condensate material properties, the measured membrane voltage on human embryonic kidney (HEK) 293T cells was stable for tens of minutes until purposefully perturbed by an ejection pressure that broke the membrane seal (fig. S1B). A similar time window was maintained in cells over-expressing synapsin and α-synuclein (Fig. 1B), sufficient for extensive aspiration measurements where each pressure step takes ~10 s. In addition to membrane voltage, the fluorescence of cytosolic proteins can be used as a secondary monitor for potential leakages at the cell membrane (Fig. 1B).

In HEK 293T cells, the expression of synapsin alone was not sufficient to drive condensate formation, likely due to the lack of client proteins and other neuronal components naturally occurring to promote phase separation at the nerve terminal (*45*). Co-expressing synapsin with α-synuclein or intersectin Src homology 3 (SH3) domains robustly induced micron-sized synapsin condensates (Fig. 1C and fig. S1) (*30*). We focused our further study on a minimal system with HEK 293T cells co-expressing fluorescently tagged full-length synapsin 1 and α-synuclein due to their relevance in neurotransmission and synucleinopathies (Fig. 1C) (*30*). These cells typically have one (occasionally two) major condensate with a radius $R_c = 1.5 \pm 0.6$ μm (means ± SD, $n = 74$; fig. S1C), sufficient for accurate aspiration measurements with patch-clamp micropipettes that have an opening diameter of ~1 μm (Fig. 1D and movie S1).

After breaking into the cell but before aspirating a condensate, the electrode-containing micropipette measures the resting voltage of the cell membrane (V_{mem}; Fig. 1E). On non-transfected cells, the recorded $V_{\mathrm{mem}} = -49 \pm 6$ mV (means ± SEM, $n = 7$; fig. S1D) was consistent with membrane potentials reported for healthy HEK 293T (*46*). Cells expressing synapsin and α-synuclein showed a less polarized membrane potential ($V_{\mathrm{mem}} = -23 \pm 2$ mV; means ± SEM, $n = 47$; $P < 0.01$; fig. S1D), indicating an electrophysiological perturbation by the expressed neuronal proteins. A voltage jump (ΔV) was observed when synapsin/α-synuclein condensates entered the tip of the micropipette (Fig. 1E). The measured $\Delta V = 15 \pm 1.5$ mV (means ± SEM, $n = 41$; $P < 10^{-4}$; Fig. 1F) could be a result of either increased access resistance (fig. S2, A to D) or ionic leakage (fig. S2, E to H) due to the entrance of the condensate into the micropipette (*47*–*49*). Notably, the fluorescence of cytosolic synapsin and α-synuclein were stable during MAPAC (Fig. 1D and fig. S2), suggesting the absence of macromolecular leakage. The leakage of ions may stem from α-synuclein's ability to remodel lipid bilayers (*50*), given that ΔV was more pronounced for synapsin condensates driven by α-synuclein than for those driven by the SH3 domains of intersectin (Fig. 1G; $P < 0.01$). The robustness of MAPAC is not compromised by ionic leakage because the concentrations of intracellular ions are clamped during whole-cell patch-clamp (Supplementary Discussion). On a technical note, ΔV can be used to aid label-free detections of condensates by the micropipette tip.

Synapsin condensates in cells are viscoelastic

During MAPAC, a single cellular condensate is gently drawn into the tip of the micropipette by applying a controlled aspiration pressure (P_{asp}). We then record the length of the condensate aspirated inside the pipette (L_{p}) as a function of time (Fig. 1E and movie S1). By measuring the deformation of the condensate in response to stepwise changes in P_{asp}, we gain direct insights into whether the condensate behaves like a viscous liquid that flows like honey, an elastic solid that deforms like rubber, or a viscoelastic material that shows both viscous and elastic features (Fig. 1E and fig. S1, E to H).

Across ~100 synapsin/α-synuclein condensates in HEK 293T cells, we observed material responses ranging from apparent viscous liquid (Fig. 2A, black) to viscoelastic liquid (Fig. 2A, red) and to apparent elastic solid (Fig. 2A, blue). We found that a three-element viscoelastic liquid (Jeffreys) model is minimally required to explain all condensate responses observed in cells (Supplementary Discussion and table S1) (*51*). The model includes a viscous liquid component (η_1) that governs the long-term condensate response, in series with a viscoelastic solid component (E and η_2) that determines the short-term response (Fig. 2B) (*52*). Under constant pressure, the time-dependent L_{p} (normalized to the micropipette radius R_{p}) follows Eq. 1

$$\frac{L_{\mathrm{p}}}{R_{\mathrm{p}}} = \left(\frac{L_{\mathrm{p}}}{R_{\mathrm{p}}}\right)_0 + A\left[1 - e^{-\frac{(t-t_0)}{\tau}}\right] + B\left(t - t_0\right) \qquad (1)$$

$\left(\frac{L_{\mathrm{p}}}{R_{\mathrm{p}}}\right)_0$ is the normalized aspiration length before a stepwise pressure change at time t_0. The model has three fitting parameters: $A = \frac{P}{E}$, $B = \frac{P}{\eta_1}$, and $\tau = \frac{\eta_2}{E}$. Here, $P = P_{\mathrm{asp}} - P_{\gamma}$, and $P_{\gamma} = 2\gamma\left(\frac{1}{R_{\mathrm{p}}} - \frac{1}{R_{\mathrm{c}}}\right)$ is the capillary pressure that needs to be overcome to initiate condensate flow. In this model, an apparent elastic condensate (Fig. 2A, blue) will have an infinite viscosity, whereas an apparent viscous condensate (Fig. 2A, black) can have zero elasticity. We assigned these extreme cases using the resolution of our experiments (Supplementary Discussion). Notably, cellular condensates did not wet the inner wall of micropipettes: Condensates inside the micropipette formed a convex meniscus, could undergo necking instability, and did not leave behind any measurable fluorescence after leaving the micropipette (fig. S3). Consistent with this non-wetting contact between the condensate and the micropipette, the long-term response of L_{p} under constant pressure appeared linear (Figs. 1E and 2A) (*39*, *52*).

Next, we measured the deformation ($L_{\mathrm{p}}/R_{\mathrm{p}}$) of condensates under systematically varied steps of P_{asp} (Fig. 2C and movie S2). The slopes of "P_{asp} versus B" and "P_{asp} versus A" give η_1 and E, respectively, whereas the intercepts give P_{γ} (Fig. 2, D and E). η_1, E, and P_{γ} can then be converted to the viscosity, elasticity, and interfacial tension of the measured condensate (Supplementary Discussion) (*52*, *53*). Notably, a two-parameter linear model can be applied to the long-term response of L_{p} (Fig. 2, B and C) (*52*). The resulting P_{asp} versus B and P_{asp} versus A relations were indistinguishable from those of the full three-parameter model (Fig. 2, D and E, and fig. S4). By sacrificing the fitting for η_2 (fig. S4F), a property not directly related to the material state of the condensate (*51*), the linear model reduced fitting errors, especially for data with low signal-to-noise ratio and for data where the pressure profile significantly deviated

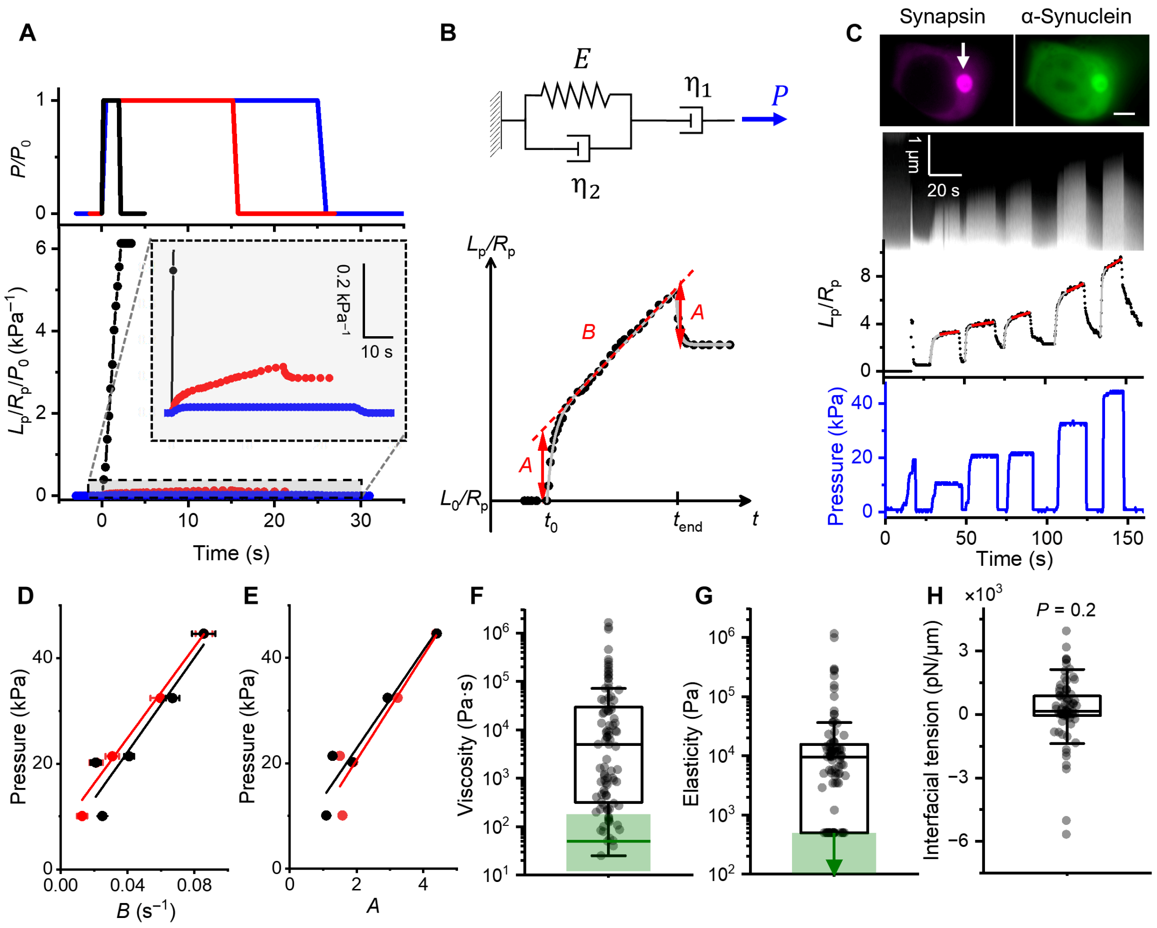

Fig. 2. Cellular synapsin condensates quantified by a three-element viscoelastic liquid model. (**A**) Representative responses of cellular synapsin condensates to a stepwise aspiration pressure. Black, apparent viscous liquid; red, viscoelastic liquid; blue, apparent elastic solid. The boxed area is magnified. (**B**) Top: The three-element viscoelastic liquid model. Bottom: Fitting of a representative condensate response to the full model (three-parameter; gray) or to a simplified linear model (two-parameter, red). *B* is the long-term shear rate; *A* is the normalized amplitude of the elastic response. (**C**) Top: Fluorescence images of a HEK 293T cell co-expressing mCherry-synapsin (magenta) and α-synuclein–Halo-JFX-646 (green); arrow points to the condensate; scale bar, 5 μm. Middle: Kymograph of the aspirated part of the condensates. Bottom: Normalized aspiration length (black) in response to stepwise aspiration pressure (blue). (**D** and **E**) Aspiration pressures (P_{asp}) plotted against either the long-term shear rate *B* (D) or the normalized amplitude of elastic response *A* (E). Black and red markers represent results from the full model and the linear model, respectively. Lines are linear fits. (**F** to **H**) Material properties of cellular synapsin condensates. Condensate viscosity (F) was calculated from the slope of (D) (*n* = 93; black). Condensate elasticity (G) was calculated from the slope of (E) (*n* = 93; black), and 24 condensates with pure viscous response were assigned an elasticity of 500 Pa (Supplementary Discussion). The viscosity of cytoplasm is plotted in green (line, median; shade, interquartile range; *n* = 7), with the arrow representing nonmeasurable elasticity. The interfacial tension of condensates (H) was calculated from the intercepts of (D) and (E) (*n* = 77). *P* value from one-sample *t* test with 0.

from a step function (fig. S4). Therefore, we used the linear model for all further analysis of cellular condensates.

Cellular synapsin condensates exhibited viscoelastic moduli that spanned more than four orders of magnitude (Fig. 2, F and G, black; *n* = 93) from pure liquid states that flow easily (viscosity $< 10^2$ Pa·s; no measurable elasticity) to apparent solid states that cannot be measurably deformed (viscosity of ~10^6 Pa·s and elasticity of ~10^5 Pa). The viscoelasticity of cellular condensates were intrinsic properties of the condensate-forming proteins, as they were not significantly affected by the choice of fluorescent tags (fig. S5, A and B) and did not depend on the resting potential of the cell (fig. S5, C to E). Furthermore, the measured viscoelasticity of synapsin/α-synuclein condensates did not correlate with either the size of the observed voltage jump (fig. S5F) or the time of each pressure step relative to the entrance of the condensate (fig. S5, G and H), confirming the lack of irreversible effects (e.g., leakage) on our MAPAC measurements. Lastly, we did not observe significant enrichment of filamentous actin around or inside synapsin/α-synuclein condensates (fig. S5, I and J), and the viscoelasticity of condensates was significantly higher than that of the surrounding cytoplasm (Fig. 2, F and G, green; *n* = 7; fig. S5K and movies S3 and S4), suggesting that our measurements of condensate viscoelasticity were not affected by the cytoskeleton.

The measured interfacial tension of cellular condensates ($\gamma = 240 \pm 220$ pN/μm; means ± SEM; Fig. 2H and fig. S6) was not significantly different from zero ($P = 0.2$), consistent with the low interfacial tension of protein condensates reported in vitro (*38*). The uncertainties in interfacial tension correspond to a capillary pressure P_γ (~1 kPa) that did not significantly affect aspiration pressures used for viscoelasticity measurements (10 to 50 kPa; Fig. 2C).

The viscosity of cellular synapsin condensates (median of 5000 Pa·s; Fig. 2F) was significantly higher than the viscosity of protein condensates observed in vitro (1 to 1000 Pa·s) (*38*, *54*). However, cellular condensates that appear highly viscoelastic may resemble disease-related solid aggregates, such as α-synuclein containing Lewy bodies (*55*, *56*). Therefore, we next explore whether the partitioning of α-synuclein plays a role in determining the viscoelasticity of synapsin condensates in cells.

Condensate partitioning of α-synuclein dictates the viscoelasticity of synapsin condensates in cells

When α-synuclein and synapsin were heterogeneously expressed in HEK 293T cells, the condensate partitioning coefficient of α-synuclein ($\Pi_{\alpha\mathrm{Syn}}$; i.e., the concentration of α-synuclein in condensates relative to that in the dilute phase) spanned two orders of magnitude, from weakly depleted from condensates ($\Pi_{\alpha\mathrm{Syn}} < 1$) to highly enriched in the condensate phase ($\Pi_{\alpha\mathrm{Syn}} > 10$; fig. S7, A to C). In comparison, the condensate partitioning coefficient of synapsin (Π_{synapsin}) was more clustered (~10) and overall higher than $\Pi_{\alpha\mathrm{Syn}}$ ($P < 10^{-4}$; fig. S7C), reminiscent of the observation of α-synuclein being a client protein recruited to condensates formed by synapsin (*30*).

For synapsin/α-synuclein condensates with comparable Π_{synapsin} (10 ± 3), we found $\Pi_{\alpha\mathrm{Syn}}$ to be an accurate prophecy of the condensate's viscoelastic response under MAPAC: Condensates with $\Pi_{\alpha\mathrm{Syn}} \sim 1$ easily flowed under pressure; the flow of $\Pi_{\alpha\mathrm{Syn}} \sim 5$ condensates was ~100 times slower, whereas condensates with $\Pi_{\alpha\mathrm{Syn}} > 10$ were barely deformable (Fig. 3A). Across 43 cells that co-expressed mCherry-synapsin and α-synuclein–Halo (stained with JFX-646), the viscoelasticity of formed condensates strongly correlated with $\Pi_{\alpha\mathrm{Syn}}$ [Fig. 3B and fig. S7D; Pearson's correlation coefficient (r) = 0.84 for viscosity and $r = 0.74$ for elasticity]. In contrast, the viscoelasticity was not dependent on the apparent concentrations of α-synuclein in the cytosol ($r = 0.08$; fig. S7E) and was only weakly dependent on the apparent concentration of α-synuclein in the condensate ($r = 0.39$; fig. S7F), consistent with the partitioning coefficient being a better indicator of α-synuclein's affinity toward the condensates (Supplementary Discussion) (*8*). Additionally, the measured viscoelasticity and partitioning coefficients were not strongly correlated with the condensate radius ($r = 0.14$ for viscosity and $r = 0.35$ for elasticity; fig. S7G), suggesting the condensates are homogeneous at the scale of MAPAC-induced deformations. Notably, fig. S7G also confirms the lack of optical artifacts induced by condensate curvature (*57*).

A positive correlation ($r = 0.68$) was observed between $\Pi_{\alpha\mathrm{Syn}}$ and Π_{synapsin} in cells (fig. S7H), indicating the presence of cellular factors that promoted heterotropic cooperativity between α-synuclein and synapsin. Consequently, Π_{synapsin} can also predict the viscoelasticity of cellular condensates (Fig. 3C and fig. S7, I to K; $r = 0.66$ for viscosity and $r = 0.60$ for elasticity) albeit less accurately compared to $\Pi_{\alpha\mathrm{Syn}}$. Condensates with $\Pi_{\alpha\mathrm{Syn}} \sim 1$ but $\Pi_{\mathrm{synapsin}} > 30$ showed strong viscoelastic features, while condensates with high values (>30) of both $\Pi_{\alpha\mathrm{Syn}}$ and Π_{synapsin} were not measurably deformable (Fig. 3D). Linear combinations of $\Pi_{\alpha\mathrm{Syn}}$ and Π_{synapsin} did not outperform $\Pi_{\alpha\mathrm{Syn}}$ alone in predicting the viscoelasticity of cellular condensates (fig. S7L), consistent with the partitioning of α-synuclein being the main driver for the viscoelasticity of synapsin condensates in cells.

Synapsin domains and crowding conditions regulate the viscosity and interfacial tension of synapsin condensates

To verify the effect of α-synuclein and to explore additional regulators on the material properties of synapsin condensates, next, we explore synapsin condensates reconstituted in vitro (*23*). Full-length synapsin 1 (hereafter named "FL synapsin") comprises a membrane-binding domain and an adenosine 5′-triphosphate (ATP)–binding domain at the N terminus, with an IDR at the C terminus (Fig. 4A) (*23*, *28*). Purified FL synapsin spontaneously forms condensates under physiologically relevant conditions: 5 to 10 μM synapsin in 150 mM NaCl, 3 to 10% PEG, molecular weight 8000 (PEG-8000; hereafter named "PEG"), pH 7.4. While our cellular measurements (Figs. 1 to 3) focused on FL synapsin, in vitro studies have identified the IDR to be the main driver of the phase separation of synapsin: Deleting the IDR abolishes phase separation, while the purified IDR fragment can form condensates on its own (*23*). However, it is unclear whether condensates formed by the IDR are distinct, in their material properties, from those consisting of FL synapsin.

Using an optical tweezers-assisted droplet fusion assay (Fig. 4B) (*38*, *41*), we found that the capillary velocity of IDR condensates (13.0 ± 0.6 μm/s) was more than 10 times faster than that of FL condensates (0.8 ± 0.1 μm/s; Fig. 4C; both under 10% PEG). Reducing the amount of PEG from 10 to 3% minimally affected the capillary velocity of FL synapsin condensates (Fig. 4, B and C). Unlike synapsin FL, IDR did not form condensates under 3% PEG (fig. S8, A to D). IDR's lower–phase separation propensity as compared to FL is consistent with the lack of condensates in HEK 293T cells that overexpress fluorescently tagged synapsin IDR and α-synuclein.

The capillary velocity, which reports a ratio of interfacial tension to viscosity of the studied condensates, does not provide a direct measure of either material property (*41*). To address this, we applied MPA to synapsin condensates. All reconstituted synapsin condensates wetted the inner wall of micropipettes (Fig. 4D) and the aspiration length (L_{p}) changed with the square root of time (fig. S8E). Consistent with the droplet fusion assay (Fig. 4C), the responses of reconstituted synapsin condensates were not significantly different from those predicted for purely viscous liquids (*39*), suggesting condensate elasticities below 10 Pa (Supplementary Discussion). By analyzing synapsin condensates under various aspiration pressures (P_{asp}; Fig. 4E), we observed linear relations between the aspiration pressure and the effective shear rate (S; Fig. 4F). The slope of P_{asp} versus S reports condensate viscosity (η; Fig. 4G), while the intercept reports the interfacial tension of condensates (γ; Fig. 4H).

Under the same crowding condition (10% PEG), the viscosity of IDR condensates (η = 12.9 Pa·s; median, same below) was about 10 times lower than that of FL condensates (112 Pa·s; $P < 10^{-4}$), whereas the interfacial tensions (γ) of the two types of condensates were comparable ($P = 0.05$). These results are consistent with the ~10-fold faster capillary velocity (γ/η) of IDR than that of FL synapsin condensates (Fig. 4C). However, with direct measurements by MPA, we now assign a clear role of the synapsin N-terminal region as a mediator of the condensate's viscosity, rather than their interfacial tension. The ~10-fold difference between the viscosity of FL and IDR synapsin condensates is significantly larger than expectations based on the proteins' molecular mass [FL, 102.4 kDa; and IDR, 57.6 kDa; both tagged with enhanced green fluorescent protein (eGFP)] (*58*), consistent with the N-terminal region's ability to dimerize synapsin (*59*).

PEG is a commonly used crowding agent that facilitates phase separation of proteins (*60*, *61*). We observed that reducing the

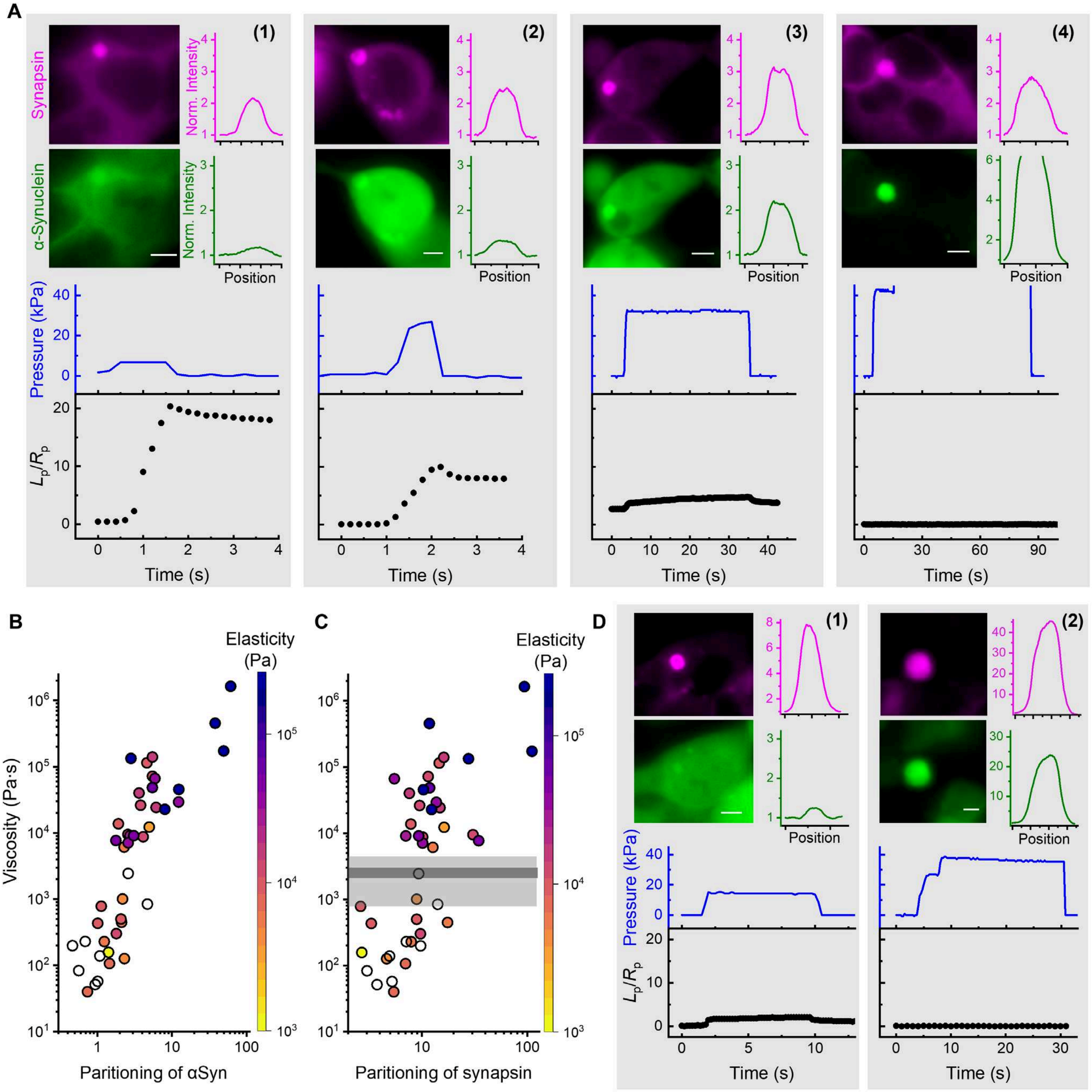

Fig. 3. The partitioning of α-synuclein dictates the viscoelasticity of synapsin condensate in cells. (**A**) Top: Wide-field fluorescence images of four HEK 293T cells co-expressing mCherry-synapsin (magenta) and α-synuclein–Halo labeled with JFX-646 (green). Fluorescence intensity profiles across the condensate are plotted on the right of each image. These four condensates have similar partitioning of synapsin but markedly different partitioning of α-synuclein, from (1) to (4): $\Pi_{\text{synapsin}} = 5.2$, 9.7, 13.7, and 11.7 and $\Pi_{\alpha\text{Syn}} = 1.0$, 1.8, 5.5, and 38, respectively. See fig. S7 for conversion from apparent partitioning measured from wide field to true partitioning measured from confocal microscopy. Bottom: Applied aspiration pressure step (blue) and corresponding response of each condensate (black). All graphs have the same scale in P_{asp} and L_p/R_p. The condensate increased in viscosity and elasticity from (1) to (4). (**B** and **C**) The relationships between the viscosity of 43 condensates as a function of $\Pi_{\alpha\text{Syn}}$ (B) or Π_{synapsin} (C). The elasticity of each condensate was colored according to the map. White condensates did not show measurable elastic response and was assigned an elasticity of 500 Pa. The gray line and shade represent the mean and SD of the system viscosity ($\eta_2/6$) measured from the full model. (**D**) Top: Wide-field fluorescence images of two HEK 293T cells co-expressing mCherry-synapsin (magenta) and α-synuclein–Halo labeled with JFX-646 (green), with fluorescence intensity profiles across the condensate plotted on the right of each image. From (1) to (2): $\Pi_{\text{synapsin}} = 35$ and 93 and $\Pi_{\alpha\text{Syn}} = 1.8$ and 61, respectively. Bottom: Applied aspiration pressure step (blue) and corresponding response of each condensate (black). Error bars are SEM. Scale bars, 5 μm.

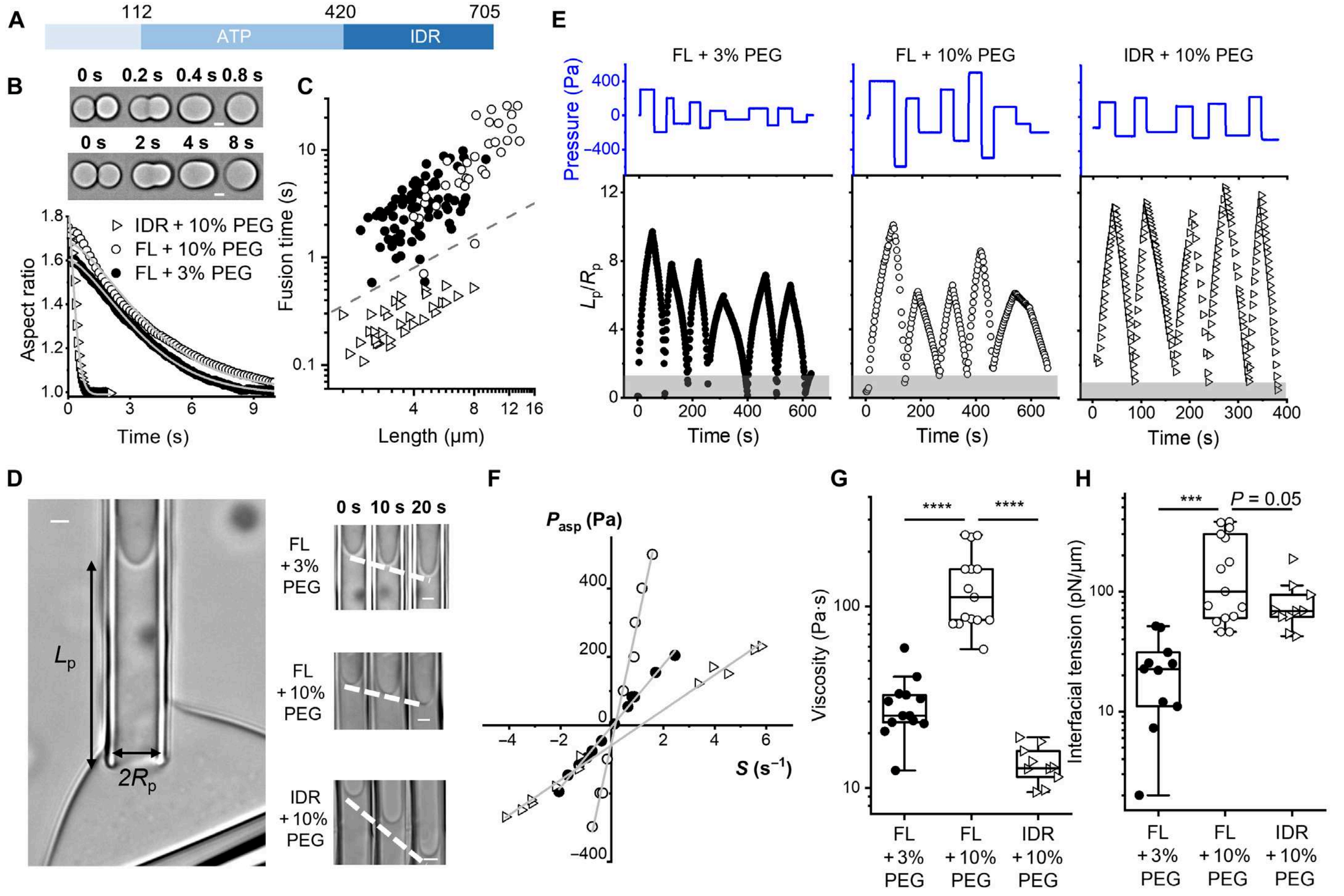

Fig. 4. PEG increases both the viscosity and interfacial tension of synapsin condensates while the IDR of synapsin maintains a low condensate viscosity. (**A**) Domain diagram of FL synapsin. (**B**) Images showing the fusion of IDR (top) and FL (middle) synapsin condensates. Bottom: The relaxation of condensate aspect ratios. Gray curves are stretched-exponential fits. Open triangles: IDR, 10% PEG; open circles: FL, 10% PEG; close circles: FL, 3% PEG; same below. (**C**) Condensate fusion time versus condensate length. Capillary velocities: 13.0 ± 0.6 μm/s [IDR + 10% PEG; coefficient of determination (R^2) = 0.93; n = 33 pairs], 0.8 ± 0.1 μm/s (FL + 10% PEG; $R^2 = 0.81$; $n = 34$ pairs), and 1.3 ± 0.1 μm/s (FL + 3% PEG; $R^2 = 0.82$; $n = 76$ pairs). The dashed line has a slope of 1. (**D**) Left: Transmitted-light image showing a micropipette-aspirated synapsin condensate (held by a second pipette). Right: Time-lapse images showing the flow of FL and IDR synapsin condensates under constant ejection pressure (top and middle: $P_{asp} = -300$ Pa; bottom: $P_{asp} = -250$ Pa). Scale bars, 2 μm. (**E**) Aspiration pressure (blue) and normalized aspiration length (black) during MPA of FL and IDR synapsin condensates. The gray shades represent $L_p/R_p < 1$. (**F**) The relationship between aspiration pressure and shear rate S, defined as $S = d(L_p/R_p)^2/dt$. Solid lines are linear fits (all $R^2 > 0.99$). (**G**) Viscosity and (**H**) interfacial tension of FL (3% PEG, $n = 13$; and 10% PEG, $n = 15$) and IDR (10% PEG, $n = 10$) synapsin condensates measured by MPA. P values determined using one-way analysis of variance (ANOVA) followed by post hoc Tukey's test. ***$P < 10^{-3}$ and ****$P < 10^{-4}$.

concentration of PEG from 10 to 3% led to significant decreases in both the viscosity (η from 110 to 25 Pa·s; $P < 10^{-4}$; Fig. 4G) and interfacial tension (γ from 100 to 23 pN/μm; $P < 10^{-3}$; Fig. 4H) of FL synapsin condensates. However, the capillary velocity (γ/η = 0.89 μm/s in 10% PEG and γ/η = 0.91 μm/s in 3% PEG) of condensates remained largely unaltered. Therefore, only measuring the capillary velocity (i.e., via droplet fusion) would have missed the significant effects of PEG on condensate material properties (for comparison, see Fig. 4C). Notably, PEG has been shown to reduce the fluidity of nucleoprotein condensates (*60*, *61*), suggesting a universal crowder-mediated intermolecular attraction in protein condensates (*60*–*63*).

α-Synuclein increases the viscosity of synapsin condensates in a self-catalytic manner

To verify the observed effect of α-synuclein on the viscoelasticity of synapsin condensates in cells (Fig. 3), we added purified α-synuclein to FL synapsin condensates in vitro. As previously reported, α-synuclein colocalized with synapsin condensates (Fig. 5A) (*30*). The partitioning of α-synuclein did not affect the wetting of condensates to micropipettes (Fig. 5B), and synapsin/α-synuclein condensates remained purely viscous within the timescale of our MPA measurements (i.e., elasticity below our detection limit of 10 Pa; Fig. 5C and fig. S9). However, the viscosity of condensates significantly increased in the presence of α-synuclein ($P < 10^{-3}$; Fig. 5D), whereas the interfacial tension of synapsin condensates was not significantly perturbed ($P = 0.08$; Fig. 5E). The effects of α-synuclein on the viscosity and interfacial tension of reconstituted synapsin condensates directly verify our observations in cells (Fig. 3B and fig. S5). The increase in condensate viscosity suggests that α-synuclein reduces the dynamics of intermolecular contacts within the condensate phase (*6*), consistent with the reported attenuation of SV recycling in neurons that overexpress α-synuclein (*31*, *37*, *64*). Notably, this effect was

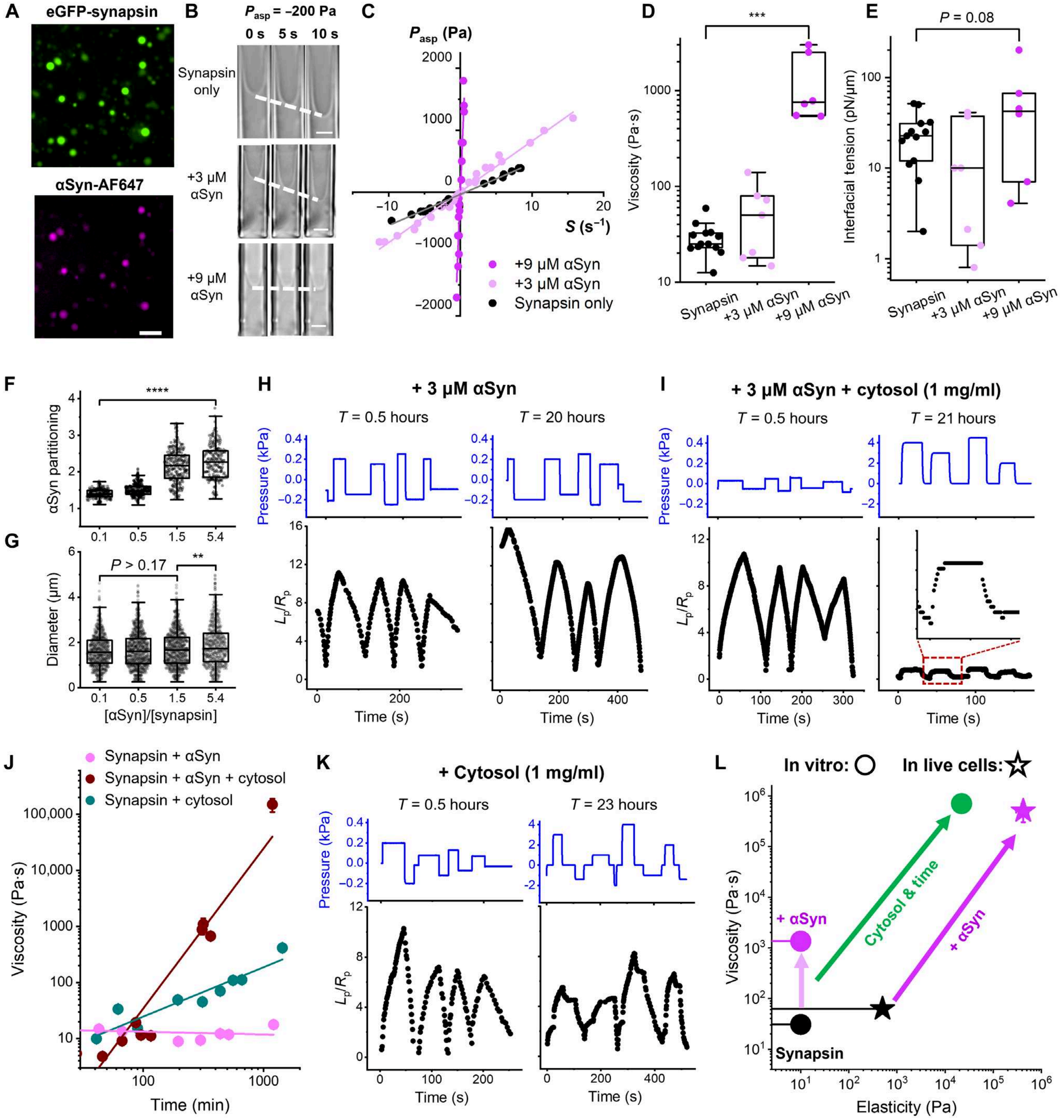

Fig. 5. α-Synuclein increases the viscosity and strengthens the maturation of FL synapsin condensates in the cytosol. (**A**) Colocalization of eGFP-synapsin (green) and α-synuclein (magenta). Scale bar, 10 μm. (**B**) Time-lapse transmitted-light images of synapsin condensate with increasing concentration of α-synuclein. Dashed lines trace the change in L_p under −200 Pa. Scale bars, 2 μm. (**C**) Relation between aspiration pressure and shear rate measured on synapsin/α-synuclein condensates. The solid lines are linear fits. Effect of α-synuclein on the viscosity (**D**) and interfacial tension (**E**) of synapsin condensates. The partitioning of α-synuclein to (**F**) and the diameter of (**G**) synapsin condensates with increasing molar ratio of α-synuclein to synapsin. (**H**) Aspiration pressure (blue) and normalized aspiration length (black) during MPA of the fresh state ($T = 0.5$ hours, time zero is the reconstitution time) and the matured state ($T = 20$ hours) of a synapsin condensate in the presence of 3 μM α-synuclein. (**I**) Same experiments as (H) except with the addition of cytosol (1 mg/ml). The zoom-in shows an elastic response of the matured condensate. (**J**) Viscosity versus time for condensates of synapsin + 3 μM α-synuclein (light magenta; $n = 3$), synapsin + 3 μM α-synuclein + cytosol (1 mg/ml; brown; $n = 4$), and synapsin + cytosol (1 mg/ml; green; $n = 3$). The solid lines are linear fits. (**K**) Same experiments as (I) except without α-synuclein. (**L**) Viscosity and elasticity of synapsin condensates. Circles represent in vitro condensates [black, synapsin only; magenta, synapsin + 9 μM α-synuclein; green, synapsin + 3 μM α-synuclein + cytosol (1 mg/ml), matured over 20 hours] with freshly prepared condensates assigned an elasticity of 10 Pa. Stars represent synapsin/α-synuclein condensates in cells with low (black) and high (magenta) partitioning of α-synuclein. *P* values determined using one-way ANOVA followed by post hoc Tukey's test. $**P < 0.01$, $***P < 10^{-3}$, and $****P < 10^{-4}$.

nonlinear: 3 μM α-synuclein caused less than twofold viscosity increase, while a ~50-fold increase in condensate viscosity was observed in the presence of 9 μM α-synuclein (Fig. 5D).

Under low concentrations of α-synuclein, the protein's affinity toward synapsin condensates can be evaluated via its condensate partitioning coefficient ($\Pi_{\alpha\mathrm{Syn}}$; Supplementary Discussion) (*8*). $\Pi_{\alpha\mathrm{Syn}}$, albeit larger than 1, was much lower than the condensate partitioning coefficient of synapsin (Π_{synapsin}) (Fig. 5F and fig. S10), consistent with the partitioning of these two proteins in cells (fig. S7C). Notably, $\Pi_{\alpha\mathrm{Syn}}$ increased with α-synuclein concentration (Fig. 5F), suggesting a homotropic cooperativity between α-synuclein molecules in their partitioning to synapsin condensates (Supplementary Discussion). Meanwhile, Π_{synapsin} remained constant with increasing amount of α-synuclein (fig. S10D). This cooperativity between α-synuclein is in line with the protein's nonlinear effect on the viscosity of synapsin condensates (Fig. 5D). The size distribution of condensates represents a balance between condensate interfacial tension and the mixing entropy of the system (*13*). The size of synapsin/α-synuclein condensates remained constant under a wide range of α-synuclein concentrations (Fig. 5G), in agreement with the lack of α-synuclein effect on the interfacial tension of synapsin condensates in vitro (Fig. 5E) and in cells (fig. S6).

Synapsin condensates significantly mature in the cytosol, accelerated by α-synuclein

The increase of synapsin condensate viscosity with the partitioning of α-synuclein in vitro (Fig. 5, D and F) qualitatively agrees with our observations in live cells (Fig. 3B). However, the "in vitro" and "in cell" results are quantitatively different: (i) The viscosity of cellular condensates (10 to 10^6 Pa·s) spanned a three-order-of-magnitude wider range as compared to that in vitro (10 to 10^3 Pa·s). (ii) Most cellular condensates showed substantial elasticity (median of 10^4 Pa), whereas condensate elasticity was not detectable in vitro (<10 Pa). These large differences directly demonstrate the importance of live cell measurements in understanding the material properties of condensates in their natural environment.

We hypothesize that two key factors could have contributed to the quantitative discrepancy between the viscoelasticity of in vitro and cellular condensates: (i) Cellular condensates (measured 18 to 24 hours post-transfection) have significantly longer maturation time as compared to in vitro condensates (measured within 2 hours of reconstitution). This maturation of cellular condensates can lead to a significantly higher viscoelasticity, similar to the "aging" of PGL-3 and Fused in Sarcoma (FUS) condensates (*5*). (ii) Cytosolic components absent from our in vitro reconstitution can significantly increase the viscoelasticity of synapsin/α-synuclein condensates.

To test these hypotheses, we extended the in vitro measurements from ~2 to >20 hours after reconstitution (Materials and Methods). We first tracked individual synapsin/α-synuclein condensates under a common experimental condition [9 μM synapsin, 3 μM α-synuclein, 3% PEG, 150 mM NaCl, 25 mM Tris-HCl, and 0.5 mM tris(2-carboxyethyl)phosphine (TCEP; pH 7.4)]. Over a 20-hour time window, we did not observe any measurable increase in condensate viscoelasticity (Fig. 5H and movie S5; viscosity of 17.9 ± 0.6 Pa·s at 0.5 hour versus 17.7 ± 1.8 Pa·s at 20 hour; non-detectable elasticity at either time point). These data suggest that maturation time alone does not explain the large discrepancy between the viscoelasticity of in vitro and cellular condensates.

Next, we investigated the role of cytosolic components by adding human cytosol (at a final concentration of 1 mg/ml) to the previous experimental condition. Freshly prepared synapsin/α-synuclein condensates in cytosol behaved as purely viscous liquid with a viscosity (~10 Pa·s) comparable to those measured in the absence of cytosol (Fig. 5I), suggesting that the cytosol does not have an acute effect on condensate viscoelasticity. However, a marked increase in the viscoelasticity of condensates was observed after extended incubation in cytosol: At ~20 hours, synapsin/α-synuclein condensates exhibited a viscosity of 10^6 Pa·s and an elasticity of 10^4 Pa (Fig. 5I and movie S6), resembling the most viscoelastic condensates observed in cells (Fig. 3B).

Notably, we found the change of condensate viscosity follows an approximate power-law over time: $\eta \sim t^{\beta}$, where the exponent "β" quantitatively describes the strength of the maturation effect. Without cytosol, the exponent for synapsin/α-synuclein condensates is indistinguishable from zero ($\beta = -0.05 \pm 0.08$). In contrast, $\beta = 2.9 \pm 0.3$ after the addition of cytosol (1 mg/ml; Fig. 5J), corresponding to a viscosity that increases approximately cubically with time. In the absence of α-synuclein, the maturation of synapsin condensates weakened to $\beta = 0.9 \pm 0.1$, with condensate viscosity increasing ~50-fold and condensate elasticity only beginning to be measurable after ~20 hours of incubation (Fig. 5K). The role of α-synuclein in promoting condensate maturation is consistent with the viscoelastic regulation of synapsin condensates by the partitioning of α-synuclein in cells (Fig. 3B).

Therefore, the partitioning of α-synuclein markedly increases the viscosity of synapsin condensates both in vitro and in living cells. However, the presence of cytosolic components and sufficient maturation time are required to bridge the gap between the viscoelasticity of condensates in vitro and in live cells (Fig. 5L).

SVs increase the viscosity but lower the interfacial tension of synapsin condensates

The main physiological role of synapsin condensates is to organize the reserve pool of SVs in the presynaptic terminal (*23*). Therefore, the material state of synapsin condensates may directly affect SV recycling and neurotransmitter release that are crucial for synaptic transmission. We found that SVs purified from rat brains (visualized with the lipophilic FM 4-64 dye) partition strongly into synapsin condensates (Fig. 6A) (*26*). Physiological concentrations of SVs [~50 nM vesicles; (*30*)] significantly increased the viscosity ($P = 0.01$) but decreased the interfacial tension ($P < 0.01$) of synapsin condensates (Fig. 6, B to E, and fig. S11). The increase in condensate viscosity is consistent with SV's ability to provide multivalent interactions that promote the phase separation of synapsin. With 46 nM SVs, some synapsin/SV condensates became irregularly shaped (fig. S11B), indicating a transition into viscoelastic states for those condensates. The increase of condensate viscosity by SVs suggests that the partitioning of SVs may slow down the transport of vesicles in the reserve pool, consistent with recent single-molecular tracking measurements (*26*). The reduction in the interfacial tension agrees with SVs' tendency to enrich at the interface of synapsin condensates (*26*), indicating a role of SVs in mediating the morphological integrity of the reserve pool. Notably, measurements on condensates formed by a ternary mixture of synapsin/α-synuclein/SV suggested weak competitions between the effects of α-synuclein and SV on synapsin condensates (fig. S12).

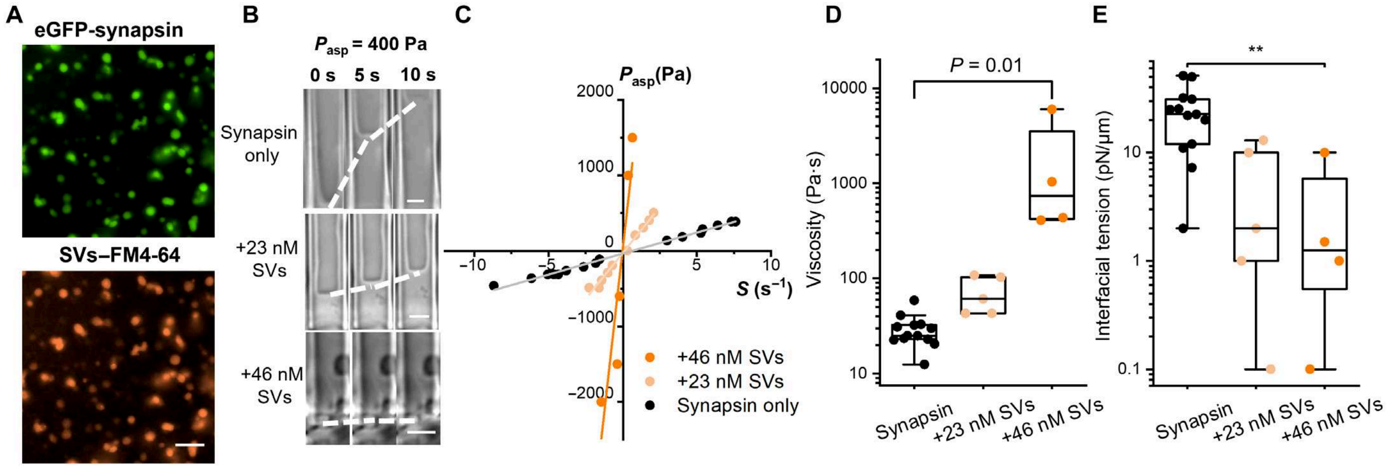

Fig. 6. SVs increase the viscosity but lower the interfacial tension of full-length synapsin condensates. (**A**) Colocalization of eGFP-synapsin (green) and SVs labeled with FM 4-64 (orange). Scale bar, 10 μm. (**B**) Time-lapse transmitted light images showing the deformation of synapsin condensates with increasing concentration of SVs. Dashed lines trace the change in L_p under 400 Pa aspiration pressure. Scale bars, 2 μm. (**C**) Relation between aspiration pressure and shear rate measured on condensates of synapsin only (black), synapsin + 23 nM SVs (light orange), and synapsin + 46 nM SVs (orange). Effect of SVs on the viscosity (**D**) and interfacial tension (**E**) of synapsin condensates. *P* values determined using one-way ANOVA followed by post hoc Tukey's test. $^{**}P < 0.01$.

DISCUSSION

MAPAC allowed us to carry out the first direct quantitative study of the material properties of condensates in living cells. We found that the viscoelasticity of cellular synapsin condensates spanned more than four orders of magnitude (Fig. 2) but was highly correlated with the partitioning of α-synuclein (Fig. 3). Coordinated with in vitro reconstitutions (Fig. 5), we identified a critical role of α-synuclein in directly regulating the material properties of synapsin condensates (Fig. 7A). Our results opened the door to understanding α-synuclein's roles in regulating the dynamics of SV and neurotransmitter release (*30*, *31*, *37*, *64*) and in mediating the formation of solid aggregates that are relevant to neurodegenerative diseases (e.g., Lewy bodies in Parkinson's disease) (*55*, *56*, *65*–*67*).

Cellular synapsin condensates exhibit significantly higher elasticity than those freshly reconstituted in vitro (Fig. 5L). The elasticity values of typical cellular synapsin/α-synuclein condensates resemble those of hydrogels formed by FUS and heterogeneous nuclear ribonucleoprotein A (hnRNPA) (~10^4 Pa) (*68*, *69*), with the lowest elasticity values corresponding to purely liquid droplets and the highest elasticity values approaching those of rubber-like elastomeric proteins such as spider silk (>10^6 Pa) (*70*) and amyloid fibers of α-synuclein (~10^9 Pa) (*71*). Notably, the elasticity of cellular synapsin condensates (Fig. 2E) span a similar range as the stiffness of extracellular matrices (soft matrix of ~10^2 Pa and stiff matrix of >10^4 Pa) that can guide cell migration and differentiation (*72*), suggesting a broad mechanobiological role of biomolecular condensates.

Our in vitro study also identified that both cytosolic components and maturation time are critical in bridging the viscoelastic differences between in vitro and cellular synapsin/α-synuclein condensates (Fig. 5L). While this maturation effect may depend on the type and concentration of the cytosol, neither maturation time nor cytosol alone could significantly increase condensate viscoelasticity under our experimental conditions (Fig. 5J). However, the cytosol provides an environment in which synapsin condensates significantly mature over time. This synergistic effect is further amplified by the presence of α-synuclein, allowing purely viscous condensates to mature into near elastic solids after ~20 hours of incubation in cytosol. Cytosolic components, such as reactive oxygen species and kinases, may change the oxidation or phosphorylation state of condensate proteins, leading to the crosslinking of condensate components that exemplify as a maturation (or aging) phenomenon in which the viscoelasticity of condensates significantly increases over time. An exciting future direction would focus on identifying the exact molecular factors in the cytosol that promote the maturation of synapsin condensates.

Our measurements of cellular synapsin condensates also show that the morphology of condensates [such as sphericity; (*73*)] carries little information about their material properties. Although the majority of synapsin condensates were spherical, their viscoelasticity varied markedly, from low-viscosity liquid that allows dynamic molecular exchange to apparent solid that resembles disease-associated inclusions, such as Lewy bodies (Fig. 3) (*55*, *56*, *65*). Unlike condensate morphology, the partitioning of key regulatory proteins (i.e., α-synuclein) can be an accurate predictor of condensate material properties (Fig. 7A). Our cellular experiments were performed with the same cell line (HEK 293T), in a relatively narrow time window (18 to 24 hours post-transfection). However, subtle variations in cellular components and maturation time can still result in substantial noise in the observed correlation between the viscoelasticity of condensates and the partitioning of α-synuclein (Fig. 3B). Posttranslational modifications such as phosphorylation may provide an additional layer of viscoelastic regulation. This is particularly relevant in the case of synaptic activity, where upon activation a global series of phosphorylation events targets numerous proteins (*74*, *75*), including synapsin 1 and α-synuclein (*76*, *77*). These phosphorylation events may affect the clustering of SVs in vertebrate synapses (*35*, *77*, *78*), further emphasizing the need for methods that allow direct in vivo quantification of viscoelasticity. To fully understand synapsin biology, future efforts need to focus on exploring the roles of SVs, disease-related α-synuclein mutations, posttranslational modifications, maturation time, and other cellular components in

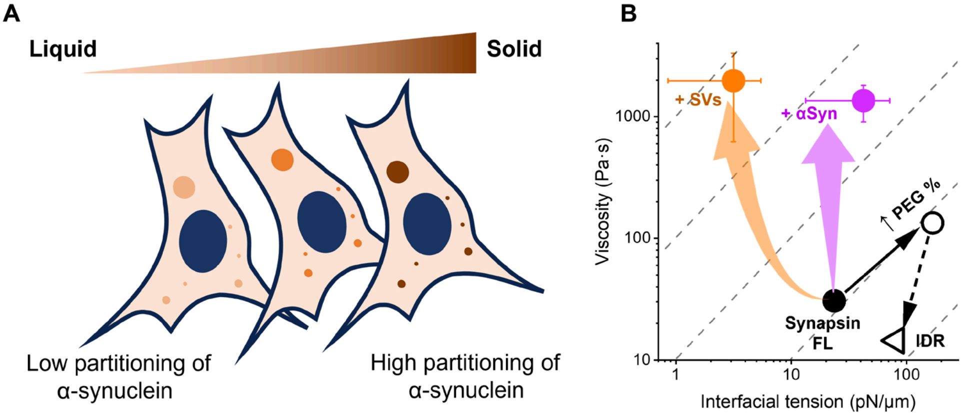

Fig. 7. The regulation of synapsin condensate material properties in vitro and in live cells. (**A**) An illustration showing that the partitioning of α-synuclein dictates the material state of synapsin condensates in cells. (**B**) Viscosity and interfacial tension of in vitro synapsin condensates. Closed circles represent FL only (black), FL + 9 μM α-synuclein (magenta), or FL + 46 nM SVs (orange) in 3% PEG. Open markers represent FL (circle) and IDR (triangle) in 10% PEG. Error bars are SEM. Each dashed line corresponds to a constant capillary velocity (i.e., interfacial tension/viscosity).

modulating the material properties of synapsin condensates under physiological or pathological conditions.

The liquidity of freshly prepared synapsin condensates can be fully controlled via biologically relevant factors in vitro. The presence of α-synuclein, SVs, and PEG (mimicking the crowding condition of the cytoplasm) all render synapsin condensates more viscous while removing the N-terminal regions of synapsin reduces condensate viscosity (Fig. 7B). Viscosity is a kinetic parameter that is governed by the dynamics of molecular interactions within the condensate (*6*), whereas interfacial tension is a thermodynamic parameter that depends on both the dense and the dilute phases (*9*). While factors that promote the phase separation of synapsin condensates generally increase condensate viscosity, they can have distinct effects on the interfacial tension of condensates: PEG increases, whereas SVs decrease the interfacial tension of synapsin condensates (Fig. 7B), highlighting the complexity of condensate interfaces (*79*). The reduction of interfacial tension by SVs is in line with the effect of protein clusters that serve as Pickering agents (*16*) and with recent observations that lipid vesicles are prone to perturb the interface of condensates (*80*).

We did not observe statistical differences between the interfacial tension of synapsin/α-synuclein condensates in vitro and in cells (Fig. 5E and fig. S5). However, the large variation and ~10-fold higher mean value of the interfacial tension of cellular condensates may reflect biomolecular assemblies (e.g., cytoskeleton) at the condensate interface that resisted the initial condensate deformation under MAPAC (*81*). Notably, a higher interfacial tension of cellular condensates may also suggest that the intracellular environment is more crowded than the reconstituted condition in vitro (3% PEG for synapsin/α-synuclein condensates; Fig. 4H).

While the viscosity of cellular condensates can be estimated via molecular diffusion measurements (e.g., FRAP, FCS, and single-molecule tracking), assumptions of molecular size, shape, and boundary conditions are needed to convert the measured diffusion coefficient to a nanoscale viscosity of the condensate (*82*). Viscosities at the nanoscale often significantly differ from the condensate's bulk rheology (*8*, *83*). The MAPAC platform described here directly measures the overall viscoelasticity of single condensates in their native surroundings. MAPAC shares a large part of its hardware with patch-clamp, a well-established tool in electrophysiology, making it easily accessible to neuroscience, biophysics, and cell biology communities (*44*, *84*). Moreover, the electrical recording capacity of MAPAC and the ease of micropipette-based single condensate extraction (movie S4) open the door to scrutinizing the coupling between electrical, mechanical, and chemical properties of condensates in live cells (*47*–*49*). Therefore, we expect MAPAC to be a widely accessible and powerful tool for quantitative understanding of a broad range of endogenous or pathological biomolecular condensates in living organisms, from p granules, stress granules, to those formed by proteins that represent hallmarks of neurodegeneration (*3*, *4*). Results from MAPAC can help illuminate the molecular mechanisms that underlie neurodegenerative diseases, reveal how compositional changes affect phase-separated structures, and identify potential therapeutic targets to restore or modulate condensate functions.

Our study of synapsin/α-synuclein condensates was carried out in a minimal system in vitro and with ectopically generated condensates in live HEK 293T cells. While these model systems allowed us to focus on dissecting molecular factors that determine the material properties of synapsin/α-synuclein condensates, future efforts will need to focus on measurements in neuronal synapses in vivo to better understand the physiological functions of these condensates. The typical opening diameter of micropipettes used in MAPAC is 0.5 to 1 μm, best suited for studying cytosolic condensates with a diameter of >1.5 μm. While micrometer-sized condensates are widely observed in the literature (54 of the 58 surveyed condensates in table S2), quantifications of submicron or nuclear condensates in live cells are still challenging. Unlike in vitro quantifications, the interfacial tension of synapsin/α-synuclein condensates in cells showed large measurement uncertainties (Fig. 2H and fig. S6). This is partly due to the low resolution of the pressure system used for cellular measurements (resolution of ~100 Pa in cell versus ~1 Pa in vitro). The compromise in resolution was needed to reach sufficiently large aspiration pressure to break into the cell and to deform the highly viscoelastic condensates (Materials and Methods). Therefore, further developments should focus on nanoscale techniques that can easily penetrate the cell surface and supply large pressure (>10 kPa) with high precision (<1 Pa).

MATERIALS AND METHODS

Cell culture and transfection

HEK 293T cells (American Type Culture Collection) were grown in Dulbecco's modified Eagle's medium (11995065, Thermo Fisher Scientific) enriched with 10% fetal bovine serum (FB12999102, Fisherbrand) and 1% penicillin-streptomycin (15140122, Thermo Fisher Scientific). Approximately 1 million cells were seeded into a 100-mm plastic dish. The cells were maintained in an environment at 37°C, with 5 to 10% CO_2 and 100% relative humidity.

A total of 300,000 cells were seeded onto a 35-mm glass bottom dish (D35-20-1.5-N, Cellvis) precoated with Matrigel Matrix (47743-715-EA, Corning Life Sciences) for transfection. Twenty-four hours after seeding the cell, a mixture of 250 μl Opti-MEM, 5 μl of P3000 reagent, 7.5 μl of Lipofectamine reagent, 1.5 μg of mCherry–synapsin 1 plasmid (*30*), and 1 μg of α-synuclein–Halo (*85*) or α-synuclein–BFP (blue fluorescent protein) (*30*) plasmid was added to the dish. Imaging and MAPAC experiments were done 18 to 24 hours after transfection. Before imaging, α-synuclein–Halo–expressing cells were incubated with 1 μM JFX-646 HaloTag Ligand (*86*) for 15 min, and the cell culture medium was replaced with an extracellular imaging buffer (XC buffer). The XC buffer contained 140 mM NaCl, 5 mM KCl, 10 mM Hepes, 10 mM glucose, 2 mM $MgCl_2$, and 2 mM $CaCl_2$, at a pH of 7.4. All chemicals were ordered from Sigma-Aldrich.

MAPAC experiments

Different from MPA measurements in vitro, micropipettes used in MAPAC were pulled into a cylindrical tip with an opening diameter of 0.5 to 1 μm (PUL-1000, World Precision Instruments). The tip was then bent to an angle of ~40° using a microforge (DMF1000, World Precision Instruments). The micropipette was filled with an intracellular buffer (126 mM K-gluconate, 4 mM KCl, 10 mM Hepes, 2 mM Mg-ATP, 0.3 mM Na_2–guanosine 5′-triphosphate, 10 mM phosphocreatine, final pH 7.2, osmolarity of 270 to 290 mosmol; all chemicals were ordered form Sigma-Aldrich) and mounted to a headstage that is connected to an Axon 700B amplifier (Molecular Devices) and to a homemade pressure recording device using an Arduino (UNO R3, ELEGOO) controlled pressure sensor (B07N8SX347, FTVOGUE, resolution of 100 Pa). The micropipette was then inserted into a dish with HEK 293T cells expressing fluorescently labeled condensates under the voltage clamp mode. Typical resistance of the micropipette was 25 to 65 megohms. A small ejection pressure (~−1 kPa) was applied to the micropipette until the pipette tip reached the targeted cell. Then, a suction pressure was maintained in the micropipette to form a giga seal near a targeted condensate. Next, the electrical recording was switched to current clamp mode (with $I = 0$) and sudden suction pressure pulses of >10 kPa were applied to break into the cell. After successfully breaking into the cell, the resting membrane voltage was recorded. On healthy HEK 293T cells, reported resting membrane voltage is around −40 mV (*46*). To characterize condensate properties under whole-cell patch-clamp mode, suction pressures were applied so that the nearby condensate could flow into the tip of the micropipette for subsequent measurements of condensate material properties. Liquid junction potentials were not compensated for in reported cell membrane potential measurements. The voltage recordings were processed through a 2-kHz filter, digitized at a rate of 10 kHz, and collected using Clampex 10.2 software (Molecular Devices).

Protein expression and purification

eGFP–synapsin 1 and eGFP–synapsin 1 IDR

Both proteins were expressed in Expi293F cells (Thermo Fisher Scientific) for 3 days following enhancement and was purified as described previously (*23*, *30*). In short, cells were lysed in a buffer that contained 25 mM Tris-HCl (pH 7.4), 300 mM NaCl, 0.5 mM TCEP (buffer A) supplemented with EDTA-free Roche cOmplete protease inhibitors, 25 mM imidazole, deoxyribonuclease I (10 μg/ml), and 1 mM $MgCl_2$. All purification steps were carried out at 4°C. Debris was removed by centrifugation for 1 hour at 20,000*g*. For affinity purification, the soluble supernatant was applied on a Ni-NTA column (HisTrapHP, Cytiva, ÄKTA pure 25M) for binding. After a wash step (buffer A with 40 mM imidazole) and elution (buffer A with 400 mM imidazole), proteins were concentrated and subjected to size exclusion chromatography (Superdex 200 Increase 10/300, GE Healthcare, ÄKTA pure 25M) in 25 mM Tris-HCl (pH 7.4), 150 mM NaCl, 0.5 mM TCEP. Proteins were snap frozen in liquid nitrogen and stored at −80°C until further use.

α-Synuclein WT and α-synuclein A140C

For condensate partitioning experiments (Fig. 5, F and G, and fig. S10), untagged human α-synuclein and α-synuclein–A140C were expressed from pET28a vector (Novagen). In brief, a 1-liter expression culture (LB; tryptone, 10 g/liter; yeast extract, 5 g/liter; and NaCl, 5 g/liter) supplemented with kanamycin (50 μg/ml) was inoculated with an overnight preculture to achieve a final optical density at 600 nm (OD_{600}) of 0.1. Cells were incubated at 37°C, and protein expression was induced at an OD_{600} of 0.7 to 0.8 with 1 mM isopropyl-β-D-thiogalactopyranoside (IPTG). Cells were shifted to 18°C and incubated overnight while shaking. Upon expression, cells were harvested by centrifugation (7000*g* for 15 min at 4°C).

For α-synuclein purification, the pellet was resuspended in 20 ml of ice-cold phosphate-buffered saline (PBS; Gibco, 10010015) supplemented with protease inhibitors (cOmplete EDTA-free, Roche) and a spatula tip of lysozyme (A3711, AppliChem). Suspension was subjected to lysis in a French press. The lysate was cleared by centrifugation (30 min at 50,000*g* at 4°C). Nucleic acids were precipitated by adding streptomycin sulfate (S6501, Sigma-Aldrich) to a final concentration of 10 mg/ml with constant agitation for 30 min at room temperature.

For purification of the α-synuclein–A140C variant, 1 mM dithiothreitol (DTT) was added. Subsequently, the nucleic acids were pelleted by centrifugation (30 min at 50,000*g* and at 4°C). The supernatant was transferred to a clean glass beaker, and proteins were precipitated by slowly adding ammonium sulfate to a final concentration of 0.36 g/ml with constant agitation for 60 min at 4°C. Proteins were collected by centrifugation for 30 min at 50,000*g* (4°C). The pellet was resuspended in 10 ml of PBS and boiled for 20 min. After centrifugation (30 min at 50,000*g*, 4°C), the α-synuclein containing supernatant was subjected for dialysis against 5 liters of 15 mM Tris base solution overnight (132655T, Spectrum Labs Spectra/Por1, 6- to 8-kDa MWCO Standard RC). For dialysis and subsequent ion exchange chromatography of α-synuclein–A140C variant, 1 mM DTT (final concentration) was used in all steps. The dialyzed protein solution was subjected to anion exchange chromatography (HiPrep Q FF 16/10, Cytiva, ÄKTA pure 25M) in 25 mM Tris-HCl [pH 7.7; Ion Exchange Chromatography (IEX) Buffer]. Elution was performed stepwise against 25 mM Tris-HCl (pH 7.7) containing 500 mM NaCl (IEX-HIGH). First, unwanted material was washed out with 30% IEX-HIGH. Second, α-synuclein was eluted with 50% IEX-HIGH (=250 mM NaCl). Elution fractions were analyzed by SDS–polyacrylamide gel electrophoresis (18% gel). Fractions containing α-synuclein were concentrated (Amicon Ultra 4 3-kDa MWCO, Merck Millipore) and subjected to size exclusion chromatography (Superdex 200 Increase 10/300, GE Healthcare, ÄKTA pure 25M) in 25 mM Tris-HCl (pH 7.4), 150 mM NaCl, and 0.5 mM TCEP. α-Synuclein concentration was determined at 280 nm by using a molar extinction coefficient of 5960 M^{-1} cm^{-1}. Proteins were snap frozen in liquid nitrogen and stored at −80°C until further use.

For MPA measurements (Fig. 5, A to E and H to J, and fig. S9), α-synuclein was expressed using the pT7-7 α-synuclein wild-type (WT) vector (Addgene, no. 36046) in BL21(DE3) bacteria [New England Biolabs (NEB)]. Briefly, 50 ml of starter cultures of LB medium (Thermo Fisher Scientific, BP1426-2) with ampicillin (50 μg/ml; Thermo Fisher Scientific, BP1760) were inoculated with freshly picked colonies and grown overnight (37°C, 160 rpm). The starter cultures were used to inoculate 1-liter flasks of fresh LB with ampicillin and grown at 37°C (180 rpm) until the OD_{600} measured 0.6 to 0.8. Expression was induced with 1 mM IPTG (Teknova, I3325) and grown in the incubator overnight (20°C, 160 rpm), after which cells were subsequently harvested by centrifugation (4000 rpm, 4°C, 30 min) and stored at −80°C until use.

α-Synuclein–A140C was generated from the pT7-7 α-synuclein WT vector using the Q5 Site-Directed Mutagenesis Kit (NEB, E0554) according to the manufacturer's instructions. Primers were designed using the NEBaseChanger tool, and the sequences used were as follows: 5′-CGAACCTGAATGCTAAGAAATATCTTTGC-3′ and 5′- TAGTCTTGATACCCTTCC-3′.

α-Synuclein purification was accomplished by suspension of the bacterial pellet in fresh PBS (Thermo Fisher Scientific, BP2944), followed by sonication on ice (15 s on, 30 s off; eight cycles total). The solution was then boiled, followed by centrifugation to clear the lysate (20,000 rpm, 4°C, 30 min). Streptomycin sulfate (Thermo Fisher Scientific, BP910-50) was added to the supernatant to a final concentration of 10 mg/ml and mixed at 4°C for 30 min, followed by centrifugation using the same conditions as before. The protein was precipitated from the supernatant by adding ammonium sulfate (Thermo Fisher Scientific, BP212-212) to a final concentration of 0.361 g/ml and mixing at 4°C for 1 hour. The protein was pelleted by centrifugation, and the protein pellet was resuspended in buffer A [32.2 mM Tris base (pH 7.8)]. α-Synuclein was purified via fast protein liquid chromatography (Cytiva ÄKTA Pure) using HiTrap Q HP anion exchange columns (Cytiva) and eluted at 50% buffer B [32.2 mM Tris base and 500 mM NaCl (pH 7.8)]. Final proteins were aliquoted, flash frozen in liquid nitrogen, and stored at −80°C until use. α-Synuclein-A140C was purified in the same way as described above, but with the addition of 1 mM DTT.

To label α-synuclein–A140C, first, the protein solution was centrifuged at 16,000*g* for 30 min with a 3-kDa cutoff filter (Amicon Ultra Centrifugal Filter, 3-kDa MWCO, Merck Millipore) to remove previous buffer. The centrifugation step was repeated, when necessary, to reach a targeted protein concentration of 2 mg/ml in PBS. Next, the protein solution was centrifuged at 16,000*g* for 10 min with a 100-kDa cutoff filter (Amicon Ultra Centrifugal Filter, 100-kDa MWCO, Merck Millipore) to remove potential protein aggregations. Then, the protein solution was incubated with 2× excess Alexa Fluor 647 C2 Maleimide (Invitrogen) for 2 hours at room temperature. Next, the protein dye mixture was passed through a desalting column (Zeba Spin Desalting Columns, Thermo Fisher Scientific) to remove excess dye. The concentration of labeled protein and degree of labeling were determined by NanoDrop (Invitrogen NanoDrop One, Thermo Fisher Scientific). WT α-synuclein was mixed with Alexa Fluor 647–labeled α-synuclein–A140C in a 10:1 ratio in all in vitro measurements involving fluorescently labeled α-synuclein.

Preparation of cytosol and SVs

To test the effect of cytosol on the synapsin condensates, commercially available human cytosol (Gibco, no. HMCYPL) was used to mix with synapsin. The cytosol was stored at −80°C until use. Before the sample preparation, the cytosol was quickly thawed in 37°C water bath and then put on ice before mixing with other in vitro components.

SVs were isolated according to previous publications (*30*). Briefly, 20 rat brains were homogenized in ice-cold sucrose buffer [320 mM sucrose and 4 mM Hepes-KOH (pH 7.4) supplemented with 0.2 mM phenylmethylsulfonylfluoride and pepstatin A (1 mg/ml)]. Debris was removed by centrifugation (10 min at 900*g*, 4°C), and the resulting supernatant was further centrifuged (10 min at 12,000*g*, 4°C). The pellet containing synaptosomes was washed once, and synaptosomes were lysed by hypo-osmotic shock. Free, released SVs were obtained after centrifugation of the lysate for 20 min at 20,000*g*, 4°C. The supernatant containing the SVs was further ultracentrifuged for 2 hours at 230,000*g*, resulting in a crude SV pellet. Subsequently, SVs were purified by resuspending the pellet in 40 mM sucrose followed by centrifugation for 3 hours at 110,880*g* on a continuous sucrose density gradient (50 to 800 mM sucrose). SVs were collected from the gradient and loaded to size exclusion chromatography on glass beads (300-nm diameter) and equilibrated in glycine buffer [300 mM glycine and 5 mM Hepes (pH 7.40), adjusted using KOH]. This allows for the separation of SVs from residual larger membrane contaminants. SVs were pelleted by centrifugation for 2 hours at 230,000*g* and resuspended in sucrose buffer by homogenization before being aliquoted into single-use fractions and snap frozen in liquid nitrogen until use. All animal housing and experiments were approved by the Institutional Animal Welfare Committees of the State of Berlin, Germany, and Charité University Clinic (Berlin, DE), as well as State of Lower Saxony, Germany, and Max Planck Institute for Multidisciplinary Sciences (Göttingen, DE).

Condensate fusion experiments

An optical tweezers-assisted fusion assay was carried out and analyzed following the protocol that we previously described (*38*). Two condensates were independently trapped by a pair of separate optical tweezers at minimal power (Tweez305, Aresis, Slovenia; mounted on a Nikon Ti2-A inverted microscope). The fusion events were captured at 20 Hz with a 60× water objective. MATLAB R2020b was used to analyze the captured images. The images were fitted to a Gaussian ellipse. The aspect ratio (*AR*), which is the ratio between the major and minor axes of the ellipse, was plotted over time (Fig. 4B). The time of fusion τ_{fusion} was deduced by fitting the relaxation in *AR* to a stretched exponential decay (*87*)

$$AR = \left(AR_0 - 1\right) e^{\left(-\frac{t}{\tau_{\text{fusion}}}\right)^{1.5}} + 1$$

The condensates' length was designated as the geometric mean of the condensate diameters before fusion. The ratio of viscosity over interfacial tension was calculated from the slope of the fusion time versus length (Fig. 4C).

MPA experiments in vitro

The MPA experiments were carried out on a Ti2-A inverted fluorescence microscope (Nikon, Japan) equipped with a motorized stage and two motorized four-axis micromanipulators (PatchPro-5000, Scientifica) and a multi-trap optical tweezers (Tweez305, Aresis, Slovenia) according to the protocol that we reported previously (*38*) with minor modifications. Micropipettes were made by pulling glass capillaries using a pipette puller (PUL-1000, World Precision Instruments). The pipette tip was then cut to achieve an opening diameter ranging from 2 to 5 μm. Subsequently, the pipette was bent to an angle of ~40° using a microforge (DMF1000, World Precision Instruments), as shown in fig. S1A.

The micropipette was filled with the same buffer as the buffer for synapsin [25 mM Tris-HCl, 150 mM NaCl, and 0.5 mM TCEP (pH 7.4)] using a MICROFIL needle (World Precision Instruments). The filled micropipette was then mounted onto a micromanipulator. The rear end of the pipette was connected to an automatic pressure controller (Flow-EZ, Fluigent; pressure resolution of 1 Pa). The MPA experiments were conducted in glass-bottom dishes (D35-20-1.5-N, Cellvis), under bright-field illumination to minimize potential artifacts associated with fluorescence excitation. Fluorescence images were taken after MPA experiment to confirm the protein species. Typically, optical tweezers-assisted condensate fusion experiments were first carried out to achieve a large (>5 μm) condensate for easier MPA measurements and analysis. A secondary micropipette was used to hold the condensate during MPA. To minimize sample evaporation, 1.5 ml of Milli-Q water was added to the edge of the dish. The dish and the micropipettes were covered with a thin plastic wrap (Stretch-tite, Kirkland) to minimize air exchanging between the sample and the environment. The same micropipettes were used to track a condensate for long period of time (~20 hours).

We observed that in vitro synapsin condensates always wet the inner wall of uncoated micropipettes. Therefore, the analysis of the MPA data follows the protocol described in reference (*39*). Briefly, normalized aspiration length (L_p/R_p) was segmented according to the pressure steps. For each segment, the slope of a linear fitting of $(L_p/R_p)^2$ versus time gives the effective shear rate S. Then, the slope of P_{asp} versus S gives the 4η, and the intercept gives $2\gamma/R_p$. All in vitro MPA measurements were done with 9 μM FL synapsin in 3% PEG, 150 mM NaCl, 25 mM Tris-HCl, and 0.5 mM TCEP (pH 7.4), except that 9 μM IDR and/or 10% PEG were used in noted conditions of Fig. 4 and additional components were included as noted in Figs. 5 and 6.

Condensate partitioning measurement

For in vitro partitioning measurements (Fig. 5, F and G, and fig. S10), eGFP–synapsin 1, PEG-8000, sample buffer, and (if required) maleimide-labeled α-synuclein (A140C)–647 were mixed in a reaction tube (final volume of 10 μl). From there, the sample was pipetted onto a glass bottom microscopy dish for imaging immediately. The sample solution consisted of 5 μM FL synapsin, 3% PEG, 150 mM NaCl, 25 mM Tris-HCl, and 0.5 mM TCEP, (pH 7.4) with varying concentrations of α-synuclein (A140C)–647 as indicated in the section "α-Synuclein increases the viscosity of synapsin condensates in a self-catalytic manner" and the corresponding figures (Fig. 5, F and G, and fig. S10). Each condition was assessed in at least three independent reconstitutions.

The microscopy data were acquired at the Advanced Biomedical Imaging (AMBIO) Facility at Charité Medical Center, using the Eclipse Ti Nikon Spinning Disk Confocal CSU-X, equipped with 2 EM-CCD cameras (Andor iXon 888-U3 ultra EM-CCD), Andor Revolution SD System (CSU-X), objectives PL APO 60/1.4 numerical aperture (NA) oil immersion lens. *Z*-stacks (step size, 0.3 μm) were acquired with piezo stage *z*-motor at two different wavelengths [488 nm for eGFP–synapsin 1 and 638 nm for α-synuclein (A140C)–647] after loading the sample onto the surface of the microscopy dish over a duration of 15 min. Each *z*-series was imaged twice at two different laser intensities. The lower intensity was always used for the analysis. The exposure times were set to 200 ms (488 nm) and 100 ms (638 nm), and the electron multiplying (EM) gain (30 MHz at 16-bit) multiplier was set to 300 during all these experiments. NIS Elements 5.21.02 software was used to acquire the microscopy data. Fiji ImageJ [National Institutes of Health (NIH)] was used to analyze the data.

For the diameter analysis, the equatorial *z*-plane of most condensates was selected. Then, the area (square micrometers) of all condensates within 60 μm of the edge of the sample solution was quantified by applying a Gaussian blur (Sigma: 2.00 pixels) and generating a binary image using the Otsu algorithm, based on the images from the synapsin channel. Only particles with a circularity of ≥0.9 were included in the analysis. The diameter of the analyzed condensates was calculated on the basis of the measured area.

For the analysis of the raw and relative fluorescence intensities (partitioning coefficient), a squared section of ~40 μm by 40 μm was generated, and the equatorial *z*-plane was chosen for analysis. Here, the regions of interest (ROIs) were selected by applying a Gaussian blur (Sigma: 2.00 pixels) and generating a binary image using the Otsu algorithm, based on the images from the synapsin channel, only including particles with a circularity of ≥0.9 in the analysis. Then, 10 additional ROIs of similar size to the condensates were placed in the dilute phase on the same *z*-plane, and the mean fluorescent intensities for each ROI (both condensates and dilute phase) were measured at both wavelengths. A correction value, accounting for the background fluorescence detected by the camera in the absence of any fluorophore, was subtracted from every readout value, and the mean-corrected fluorescence intensities were calculated for both channels in the condensates and the dilute phase. The partitioning coefficients for both proteins were computed by dividing each condensate's corrected mean fluorescence intensity by the mean-corrected fluorescence intensity in the dilute phase for the same corresponding image.

For the partitioning coefficient of cellular condensates, first confocal and wide-field fluorescence images of the same condensate-containing HEK 293T cells were taken on a Zeiss Axio Observer 7 inverted microscope equipped with an LSM900 laser scanning confocal module and using a 63×/1.4 NA plan-apochromatic, oil-immersion objective. The images were then analyzed using ImageJ. As shown in fig. S7A, the condensate partitioning coefficient (Π) is defined as the background-corrected mean fluorescence of in the condensate ($I_{condensate}$) divided by the background-corrected mean fluorescence of the surrounding cytosol ($I_{cytosol}$) for the studied proteins. The background was measured as the mean extracellular fluorescence

$$\Pi = \frac{I_{\text{condensate}} - I_{\text{background}}}{I_{\text{cytosol}} - I_{\text{background}}}$$

The partitioning coefficients measured with confocal and wide-field microscopy for the same condensates were used to establish a conversion function between Π_{confocal} and $\Pi_{\text{wide-field}}$ (fig. S7B). The conversion function ($\Pi_{\text{confocal}} = 6.7\Pi_{\text{wide-field}} - 5.7$) was used to assign pseudo-confocal partitioning coefficients on condensates measured in MAPAC with a wide-field configuration.

Supplementary Materials

The PDF file includes:

Supplementary Discussion
Figs. S1 to S12
Table S1
Legends for movies S1 to S6
Legend for table S2
References

Other Supplementary Material for this manuscript includes the following:

Movies S1 to S6
Table S2

REFERENCES AND NOTES

1. Y. Shin, C. P. Brangwynne, Liquid phase condensation in cell physiology and disease. *Science* **357**, (2017).
2. S. F. Banani, H. O. Lee, A. A. Hyman, M. K. Rosen, Biomolecular condensates: Organizers of cellular biochemistry. *Nat. Rev. Mol. Cell Biol.* **18**, 285–298 (2017).
3. S. Alberti, D. Dormann, Liquid–liquid phase separation in disease. *Annu. Rev. Genet.* **53**, 171–194 (2019).
4. C. Mathieu, R. V. Pappu, J. P. Taylor, Beyond aggregation: Pathological phase transitions in neurodegenerative disease. *Science* **370**, 56–60 (2020).
5. L. Jawerth, E. Fischer-Friedrich, S. Saha, J. Wang, T. Franzmann, X. Zhang, J. Sachweh, M. Ruer, M. Ijavi, S. Saha, J. Mahamid, A. A. Hyman, F. Jülicher, Protein condensates as aging Maxwell fluids. *Science* **370**, 1317–1323 (2020).
6. D. Sundaravadivelu Devarajan, J. Wang, B. Szała-Mendyk, S. Rekhi, A. Nikoubashman, Y. C. Kim, J. Mittal, Sequence-dependent material properties of biomolecular condensates and their relation to dilute phase conformations. *Nat. Commun.* **15**, 1912 (2024).
7. L. Wang, K. Choi, T. Su, B. Li, X. Wu, R. Zhang, J. H. Driskill, H. Li, H. Lei, P. Guo, E. H. Chen, Y. Zheng, D. Pan, Multiphase coalescence mediates Hippo pathway activation. *Cell* **185**, 4376–4393.e18 (2022).
8. B. S. Visser, W. P. Lipiński, E. Spruijt, The role of biomolecular condensates in protein aggregation. *Nat. Rev. Chem.* **8**, 686–700 (2024).
9. B. Gouveia, Y. Kim, J. W. Shaevitz, S. Petry, H. A. Stone, C. P. Brangwynne, Capillary forces generated by biomolecular condensates. *Nature* **609**, 255–264 (2022).
10. R. S. Fisher, S. Elbaum-Garfinkle, Tunable multiphase dynamics of arginine and lysine liquid condensates. *Nat. Commun.* **11**, 4628 (2020).
11. D. Zwicker, L. Laan, Evolved interactions stabilize many coexisting phases in multicomponent liquids. *Proc. Natl. Acad. Sci.* **119**, e2201250119 (2022).
12. S. Choi, M. O. Meyer, P. C. Bevilacqua, C. D. Keating, Phase-specific RNA accumulation and duplex thermodynamics in multiphase coacervate models for membraneless organelles. *Nat. Chem.* **14**, 1110–1117 (2022).
13. U. Rana, K. Xu, A. Narayanan, M. T. Walls, A. Z. Panagiotopoulos, J. L. Avalos, C. P. Brangwynne, Asymmetric oligomerization state and sequence patterning can tune multiphase condensate miscibility. *Nat. Chem.* **1–10**, (2024).
14. A. Cochard, M. G. Navarro, L. Piroska, S. Kashida, M. Kress, D. Weil, Z. Gueroui, RNA at the surface of phase-separated condensates impacts their size and number. *Biophys. J.* **121**, 1675–1690 (2022).
15. D. S. Banerjee, T. Chigumira, R. M. Lackner, J. C. Kratz, D. M. Chenoweth, S. Banerjee, H. Zhang, Interplay of condensate material properties and chromatin heterogeneity governs nuclear condensate ripening. bioRxiv 593010 [Preprint] (2024). https://doi.org/10.1101/2024.05.07.593010.
16. W. Folkmann Andrew, P. Andrea, C. F. Lee, S. Geraldine, Regulation of biomolecular condensates by interfacial protein clusters. *Science* **373**, 1218–1224 (2021).
17. K. Graham, A. Chandrasekaran, L. Wang, A. Ladak, E. M. Lafer, P. Rangamani, J. C. Stachowiak, Liquid-like VASP condensates drive actin polymerization and dynamic bundling. *Nat. Phys.* **19**, 574–585 (2023).
18. M. Linsenmeier, L. Faltova, C. Morelli, U. Capasso Palmiero, C. Seiffert, A. M. Küffner, D. Pinotsi, J. Zhou, R. Mezzenga, P. Arosio, The interface of condensates of the hnRNPA1 low-complexity domain promotes formation of amyloid fibrils. *Nat. Chem.* **15**, 1340–1349 (2023).
19. O. Beutel, R. Maraspini, K. Pombo-Garcia, C. Martin-Lemaitre, A. Honigmann, Phase separation of zonula occludens proteins drives formation of tight junctions. *Cell* **179**, 923–936.e11 (2019).
20. C. Akshita, H. Christian, K. A. Aleksandr, R. Jakob, K. Linda, G. Luka, R. Cristina, J. C. Emma, W. N. Jaqulin, R. Branislava, Condensates of synaptic vesicles and synapsin are molecular beacons for actin sequestering and polymerization. bioRxiv 604346 (2024). https://doi.org/10.1101/2024.07.19.604346.
21. A. Mangiarotti, N. Chen, Z. Zhao, R. Lipowsky, R. Dimova, Wetting and complex remodeling of membranes by biomolecular condensates. *Nat. Commun.* **14**, 2809 (2023).
22. J. Agudo-Canalejo, S. W. Schultz, H. Chino, S. M. Migliano, C. Saito, I. Koyama-Honda, H. Stenmark, A. Brech, A. I. May, N. Mizushima, R. L. Knorr, Wetting regulates autophagy of phase-separated compartments and the cytosol. *Nature* **591**, 142–146 (2021).
23. D. Milovanovic, Y. Wu, X. Bian, P. De Camilli, A liquid phase of synapsin and lipid vesicles. *Science* **361**, 604–607 (2018).
24. W. T. Snead, A. S. Gladfelter, The control centers of biomolecular phase separation: How membrane surfaces, PTMs, and active processes regulate condensation. *Mol. Cell* **76**, 295–305 (2019).
25. A. Yamasaki, J. M. Alam, D. Noshiro, E. Hirata, Y. Fujioka, K. Suzuki, Y. Ohsumi, N. N. Noda, Liquidity is a critical determinant for selective autophagy of protein condensates. *Mol. Cell* **77**, 1163–1175.e9 (2020).
26. C. Hoffmann, J. Rentsch, T. A. Tsunoyama, A. Chhabra, G. Aguilar Perez, R. Chowdhury, F. Trnka, A. A. Korobeinikov, A. H. Shaib, M. Ganzella, Synapsin condensation controls synaptic vesicle sequestering and dynamics. *Nat. Commun.* **14**, 6730 (2023).
27. A. Pechstein, N. Tomilin, K. Fredrich, O. Vorontsova, E. Sopova, E. Evergren, V. Haucke, L. Brodin, O. Shupliakov, Vesicle clustering in a living synapse depends on a synapsin region that mediates phase separation. *Cell Rep.* **30**, 2594–2602.e3 (2020).
28. T. C. Südhof, A. J. Czernik, H. Kao, K. Takei, P. A. Johnston, A. Horiuchi, S. D. Kanazir, M. A. Wagner, M. S. Perin, P. De Camilli, Synapsins: Mosaics of shared and individual domains in a family of synaptic vesicle phosphoproteins. *Science* **245**, 1474–1480 (1989).
29. P. Chi, P. Greengard, T. A. Ryan, Synaptic vesicle mobilization is regulated by distinct synapsin I phosphorylation pathways at different frequencies. *Neuron* **38**, 69–78 (2003).
30. C. Hoffmann, R. Sansevrino, G. Morabito, C. Logan, R. M. Vabulas, A. Ulusoy, M. Ganzella, D. Milovanovic, Synapsin condensates recruit alpha-synuclein. *J. Mol. Biol.* **433**, 166961 (2021).
31. M. Atias, Y. Tevet, J. Sun, A. Stavsky, S. Tal, J. Kahn, S. Roy, D. Gitler, Synapsins regulate α-synuclein functions. *Proc. Natl. Acad. Sci. U.S.A.* **116**, 11116–11118 (2019).
32. A. Stavsky, L. A. Parra-Rivas, S. Tal, J. Riba, K. Madhivanan, S. Roy, D. Gitler, Synapsin E-domain is essential for α-synuclein function. *eLife* **12**, RP89687 (2024).
33. M. Sharma, J. Burré, α-Synuclein in synaptic function and dysfunction. *Trends Neurosci.* **46**, 153–166 (2023).
34. K. J. Vargas, N. Schrod, T. Davis, R. Fernandez-Busnadiego, Y. V. Taguchi, U. Laugks, V. Lucic, S. S. Chandra, Synucleins have multiple effects on presynaptic architecture. *Cell Rep.* **18**, 161–173 (2017).
35. J. N. Wallace, Z. C. Crockford, C. Román-Vendrell, E. B. Brady, C. Hoffmann, K. J. Vargas, M. Potcoava, M. E. Wegman, S. T. Alford, D. Milovanovic, J. R. Morgan, Excess phosphoserine-129 α-synuclein induces synaptic vesicle trafficking and declustering defects at a vertebrate synapse. *Mol. Biol. Cell* **35**, ar10 (2024).
36. J. Diao, J. Burré, S. Vivona, D. J. Cipriano, M. Sharma, M. Kyoung, T. C. Südhof, A. T. Brunger, Native α-synuclein induces clustering of synaptic-vesicle mimics via binding to phospholipids and synaptobrevin-2/VAMP2. *eLife* **2**, e00592 (2013).
37. V. M. Nemani, W. Lu, V. Berge, K. Nakamura, B. Onoa, M. K. Lee, F. A. Chaudhry, R. A. Nicoll, R. H. Edwards, Increased expression of α-synuclein reduces neurotransmitter release by inhibiting synaptic vesicle reclustering after endocytosis. *Neuron* **65**, 66–79 (2010).
38. H. Wang, F. M. Kelley, D. Milovanovic, B. S. Schuster, Z. Shi, Surface tension and viscosity of protein condensates quantified by micropipette aspiration. *Biophys. Rep.* **100011**, (2021).
39. J. V. Roggeveen, H. Wang, Z. Shi, H. A. Stone, A calibration-free model of micropipette aspiration for measuring properties of protein condensates. *Biophys. J.* **123**, 1393–1403 (2023).
40. K. A. Ibrahim, A. S. Naidu, H. Miljkovic, A. Radenovic, W. Yang, Label-free techniques for probing biomolecular condensates. *ACS Nano* **18**, 10738–10757 (2024).
41. I. Alshareedah, G. M. Thurston, P. R. Banerjee, Quantifying viscosity and surface tension of multicomponent protein-nucleic acid condensates. *Biophys. J.* **120**, 1161–1169 (2021).
42. D. Bracha, M. T. Walls, C. P. Brangwynne, Probing and engineering liquid-phase organelles. *Nat. Biotechnol.* **37**, 1435–1445 (2019).
43. K. Ruan, G. Bai, Y. Fang, D. Li, T. Li, X. Liu, B. Lu, Q. Lu, Z. Songyang, S. Sun, Z. Wang, X. Zhang, W. Zhou, H. Zhang, Biomolecular condensates and disease pathogenesis. *Sci. China Life Sci.* **67**, 1792–1832 (2024).
44. L. S. Oliveira, A. Sumera, S. A. Booker, Repeated whole-cell patch-clamp recording from CA1 pyramidal cells in rodent hippocampal slices followed by axon initial segment labeling. *STAR Protoc.* **2**, 100336 (2021).

45. T. Yoshida, K. Takenaka, H. Sakamoto, Y. Kojima, T. Sakano, K. Shibayama, K. Nakamura, K. Hanawa-Suetsugu, Y. Mori, Y. Hirabayashi, K. Hirose, S. Takamori, Compartmentalization of soluble endocytic proteins in synaptic vesicle clusters by phase separation. *Iscience* **26**, 106826 (2023).
46. J. Chemin, A. Monteil, C. Briquaire, S. Richard, E. Perez-Reyes, J. Nargeot, P. Lory, Overexpression of T-type calcium channels in HEK-293 cells increases intracellular calcium without affecting cellular proliferation. *FEBS Lett.* **478**, 166–172 (2000).
47. Y. Dai, C. F. Chamberlayne, M. S. Messina, C. J. Chang, R. N. Zare, L. You, A. Chilkoti, Interface of biomolecular condensates modulates redox reactions. *Chem* **9**, 1594–1609 (2023).
48. C. Hoffmann, G. Murastov, J. V. Tromm, J. Moog, M. A. Aslam, A. Matkovic, D. Milovanovic, Electric potential at the interface of membraneless organelles gauged by graphene. *Nano Lett.* **23**, 10796–10801 (2023).
49. M. H. I. van Haren, B. S. Visser, E. Spruijt, Probing the surface charge of condensates using microelectrophoresis. *Nat. Commun.* **15**, 3564 (2024).
50. Z. Shi, J. N. Sachs, E. Rhoades, T. Baumgart, Biophysics of α-synuclein induced membrane remodelling. *Phys. Chem. Chem. Phys.* **17**, 15561–15568 (2015).
51. H. Zhou, Viscoelasticity of biomolecular condensates conforms to the Jeffreys model. *J. Chem. Phys.* **154**, (2021).
52. K. Guevorkian, M. Colbert, M. Durth, S. Dufour, F. Brochard-Wyart, Aspiration of biological viscoelastic drops. *Phys. Rev. Lett.* **104**, 218101 (2010).
53. J. L. Drury, M. Dembo, Hydrodynamics of micropipette aspiration. *Biophys. J.* **76**, 110–128 (1999).
54. Y. Zhang, R. Prasad, S. Su, D. Lee, H. Zhou, Amino acid-dependent material properties of tetrapeptide condensates. bioRxiv 594233 (2024). https://doi.org/10.1101/2024.05.14.594233.
55. M. C. Hardenberg, T. Sinnige, S. Casford, S. Dada, C. Poudel, E. A. Robinson, M. Fuxreiter, C. Kaminksi, G. S. Kaminski-Schierle, E. A. Nollen, C. M. Dobson, M. Vendruscolo, Observation of an α-synuclein liquid droplet state and its maturation into Lewy body-like assemblies. *J. Mol. Cell Biol.* **13**, 282–294 (2021).
56. W. S. Kim, K. Kågedal, G. M. Halliday, Alpha-synuclein biology in Lewy body diseases. *Alzheimers Res. Ther.* **6**, 73 (2014).
57. S. Yang, X. Miao, S. Arnold, B. Li, A. T. Ly, H. Wang, M. Wang, X. Guo, M. M. Pathak, W. Zhao, C. D. Cox, Z. Shi, Membrane curvature governs the distribution of Piezo1 in live cells. *Nat. Commun.* **13**, 7467 (2022).
58. P. C. Hiemenz, T. P. Lodge, *Polymer Chemistry* (CRC Press, 2007).
59. M. Hosaka, T. C. Südhof, Homo-and heterodimerization of synapsins. *J. Biol. Chem.* **274**, 16747–16753 (1999).
60. T. Kaur, I. Alshareedah, W. Wang, J. Ngo, M. M. Moosa, P. R. Banerjee, Molecular crowding tunes material states of ribonucleoprotein condensates. *Biomolecules* **9**, 71 (2019).
61. A. A. M. André, N. A. Yewdall, E. Spruijt, Crowding-induced phase separation and gelling by co-condensation of PEG in NPM1-rRNA condensates. *Biophys. J.* **122**, 397–407 (2023).
62. G. Chauhan, A. Bremer, F. Dar, T. Mittag, R. V. Pappu, Crowder titrations enable the quantification of driving forces for macromolecular phase separation. *Biophys. J.* (2023).
63. D. Qian, T. J. Welsh, N. A. Erkamp, S. Qamar, J. Nixon-Abell, G. Krainer, P. S. George-Hyslop, T. C. Michaels, T. P. Knowles, Tie-line analysis reveals interactions driving heteromolecular condensate formation. *Phys. Rev. X* **12**, 041038 (2022).
64. D. A. Scott, I. Tabarean, Y. Tang, A. Cartier, E. Masliah, S. Roy, A pathologic cascade leading to synaptic dysfunction in α-synuclein-induced neurodegeneration. *J. Neurosci.* **30**, 8083–8095 (2010).
65. D. Twohig, H. M. Nielsen, α-synuclein in the pathophysiology of Alzheimer's disease. *Mol. Neurodegener.* **14**, 23 (2019).
66. S. Ray, N. Singh, R. Kumar, K. Patel, S. Pandey, D. Datta, J. Mahato, R. Panigrahi, A. Navalkar, S. Mehra, L. Gadhe, D. Chatterjee, A. S. Sawner, S. Maiti, S. Bhatia, J. A. Gerez, A. Chowdhury, A. Kumar, R. Padinhateeri, R. Riek, G. Krishnamoorthy, S. K. Maji, α-Synuclein aggregation nucleates through liquid–liquid phase separation. *Nat. Chem.* **12**, 705–716 (2020).
67. T. E. Moors, D. Milovanovic, Defining a Lewy body: Running up the Hill of shifting definitions and evolving concepts. *J. Parkinsons Dis.* **14**, 17–33 (2024).
68. L. Guo, H. J. Kim, H. Wang, J. Monaghan, F. Freyermuth, J. C. Sung, K. O'Donovan, C. M. Fare, J. P. Taylor, J. Shorter, Nuclear-import receptors reverse aberrant phase transitions of RNA-binding proteins with prion-like domains. *Cell* **173**, 677–692.e20 (2018).
69. M. Kato, T. W. Han, S. Xie, K. Shi, X. Du, L. C. Wu, H. Mirzaei, E. J. Goldsmith, J. Longgood, J. Pei, Cell-free formation of RNA granules: Low complexity sequence domains form dynamic fibers within hydrogels. *Cell* **149**, 753–767 (2012).
70. S. Rauscher, R. Pomès, Structural disorder and protein elasticity. *Adv. Exp. Med. Biol.* **725**, 159–183 (2012).
71. K. Sweers, K. Van Der Werf, M. Bennink, V. Subramaniam, Nanomechanical properties of α-synuclein amyloid fibrils: A comparative study by nanoindentation, harmonic force microscopy, and Peakforce QNM. *Nanoscale Res. Lett.* **6**, 1–10 (2011).
72. P. A. Janmey, D. A. Fletcher, C. A. Reinhart-King, Stiffness sensing by cells. *Physiol. Rev.* **100**, 695–724 (2020).
73. J. A. Riback, J. M. Eeftens, D. S. Lee, S. A. Quinodoz, A. Donlic, N. Orlovsky, L. Wiesner, L. Beckers, L. A. Becker, A. R. Strom, Viscoelasticity and advective flow of RNA underlies nucleolar form and function. *Mol. Cell* **83**, 3095–3107.e9 (2023).
74. M. Kohansal-Nodehi, J. J. Chua, H. Urlaub, R. Jahn, D. Czernik, Analysis of protein phosphorylation in nerve terminal reveals extensive changes in active zone proteins upon exocytosis. *eLife* **5**, e14530 (2016).
75. H. Wu, X. Chen, Z. Shen, H. Li, S. Liang, Y. Lu, M. Zhang, Phosphorylation-dependent membraneless organelle fusion and fission illustrated by postsynaptic density assemblies. *Mol. Cell* **84**, 309–326.e7 (2024).
76. P. Chi, P. Greengard, T. A. Ryan, Synapsin dispersion and reclustering during synaptic activity. *Nat. Neurosci.* **4**, 1187–1193 (2001).
77. N. Ramalingam, S. Jin, T. E. Moors, L. Fonseca-Ornelas, K. Shimanaka, S. Lei, H. P. Cam, A. H. Watson, L. Brontesi, L. Ding, Dynamic physiological α-synuclein S129 phosphorylation is driven by neuronal activity. *NPJ Parkinsons Dis.* **9**, 4 (2023).
78. L. A. Parra-Rivas, K. Madhivanan, B. D. Aulston, L. Wang, D. D. Prakashchand, N. P. Boyer, V. M. Saia-Cereda, K. Branes-Guerrero, D. P. Pizzo, P. Bagchi, Serine-129 phosphorylation of α-synuclein is an activity-dependent trigger for physiologic protein-protein interactions and synaptic function. *Neuron* **111**, 4006–4023.e10 (2023).
79. Y. Zhang, A. G. Pyo, Y. Jiang, C. P. Brangwynne, H. A. Stone, N. S. Wingreen, Interface resistance of biomolecular condensates. *eLife* **12**, RP91680 (2024).
80. H. Qiu, X. Wu, X. Ma, S. Li, Q. Cai, M. Ganzella, L. Ge, H. Zhang, M. Zhang, Short-distance vesicle transport via phase separation. *Cell* **187**, 2175–2193.e21 (2024).
81. T. J. Böddeker, A. Rusch, K. Leeners, M. P. Murrell, E. R. Dufresne, Actin and microtubules position stress granules. *PRX Life.* **1**, 023010 (2023).
82. N. Taylor, S. Elbaum-Garfinkle, N. Vaidya, H. Zhang, H. A. Stone, C. P. Brangwynne, Biophysical characterization of organelle-based RNA/protein liquid phases using microfluidics. *Soft Matter* **12**, 9142–9150 (2016).
83. N. Galvanetto, M. T. Ivanović, A. Chowdhury, A. Sottini, M. F. Nüesch, D. Nettels, R. B. Best, B. Schuler, Extreme dynamics in a biomolecular condensate. *Nature* **619**, 876–883 (2023).
84. M. Garten, L. D. Mosgaard, T. Bornschlögl, S. Dieudonné, P. Bassereau, G. E. Toombes, Whole-GUV patch-clamping. *Proc. Natl. Acad. Sci. U.S.A.* **114**, 328–333 (2017).
85. J. Jackson, C. Hoffmann, E. Scifo, H. Wang, L. Wischhof, A. Piazzesi, M. Mondal, H. Shields, X. Zhou, M. Mondin, E. B. Ryan, H. Döring, J. H. M. Prehn, K. Rottner, G. Giannone, P. Nicotera, D. Ehninger, D. Milovanovic, D. Bano, Actin-nucleation promoting factor N-WASP influences alpha-synuclein condensates and pathology. *Cell Death Dis.* **15**, 304 (2024).
86. J. B. Grimm, L. Xie, J. C. Casler, R. Patel, A. N. Tkachuk, N. Falco, H. Choi, J. Lippincott-Schwartz, T. A. Brown, B. S. Glick, Z. Liu, L. D. Lavis, A general method to improve fluorophores using deuterated auxochromes. *JACS Au* **1**, 690–696 (2021).
87. A. Ghosh, H. Zhou, Determinants for fusion speed of biomolecular droplets. *Angew. Chem. Int. Ed. Engl.* **59**, 20837–20840 (2020).
88. I. Alshareedah, A. Singh, A. Quinn, P. R. Banerjee, Determinants of viscoelasticity and flow activation energy in biomolecular condensates. bioRxiv 522262 (2022). https://doi.org/10.1101/2022.12.30.522262.
89. R. M. Hochmuth, Micropipette aspiration of living cells. *J. Biomech.* **33**, 15–22 (2000).
90. C. Lin, Rethinking and researching the physical meaning of the standard linear solid model in viscoelasticity. *Mech. Adv. Mater. Struct.* **31**, 2370–2385 (2022).
91. T. Aoki, T. Ohashi, T. Matsumoto, M. Sato, The pipette aspiration applied to the local stiffness measurement of soft tissues. *Ann. Biomed. Eng.* **25**, 581–587 (1997).
92. Y. Shen, A. Chen, W. Wang, Y. Shen, F. S. Ruggeri, S. Aime, Z. Wang, S. Qamar, J. R. Espinosa, A. Garaizar, P. St George-Hyslop, R. Collepardo-Guevara, D. A. Weitz, D. Vigolo, T. P. J. Knowles, The liquid-to-solid transition of FUS is promoted by the condensate surface. *Proc. Natl. Acad. Sci. U.S.A.* **120**, e2301366120 (2023).

Acknowledgments: We thank J. Roggeveen, H. Stone, E. Dufresne, C.-Y. Lin, B. Schuster, C. Brangwynne, W. Olson, S. Khare, and members of the Rutgers Condensate journal club for helpful discussions. We thank B. Schuster lab for access to confocal microscopy. We thank L. Lavis lab for sharing JFX dyes. **Funding:** The project is supported by the National Institute of General Medical Sciences of the National Institutes of Health grant R35GM147027 (Z.S.) and by the National Institute on Drug Abuse, the National Institute of Neurological Disorders and Stroke, and the National Institute of Mental Health of the NIH under Award Number R21DA056322 (Z.S.). D.M. is supported by the start-up funds from DZNE, the research grant from the German Research Foundation (MI 2104), and the European Research Council (MEMLESSINTERFACE, 101078172); views and opinions expressed are, however, those of the authors only and do not necessarily reflect those of the European Union or the European Research Council Executive Agency; neither the European Union nor the granting authority can be held responsible for them. J.B. acknowledges NIH grant: R35GM136431. Z.P.P. acknowledges NIH grant: R21MH126420. C.H. is supported by a fellowship of the Innovative Minds Program of the German Dementia Association. X.S. is supported by a Predoctoral

Fellowship from the Autism Science Foundation. The Child Health Institute of New Jersey is partially funded by the Robert Wood Johnson Foundation (RWJF no. 74260). **Author contributions:** H.W.: Writing—original draft, conceptualization, investigation, writing—review and editing, methodology, resources, data curation, validation, formal analysis, software, and visualization. C.H.: Conceptualization, investigation, writing—review and editing, methodology, resources, data curation, validation, and formal analysis. J.V.T.: Investigation, writing—review and editing, and formal analysis. X.S.: Methodology and resources. J.E.: Writing—original draft, conceptualization, investigation, methodology, resources, and formal analysis. H.W.: Investigation and writing—review and editing. M.D.: Investigation, writing—review and editing, validation, formal analysis, and visualization. C.M.: Writing—review and editing. J.B.: Writing—review and editing, methodology, resources, funding acquisition, and supervision. Z.P.P.: Writing—review and editing, methodology, resources, funding acquisition, and supervision. D.M.: Writing—original draft, conceptualization, investigation, writing—review and editing, methodology, resources, funding acquisition, data curation, validation, supervision, formal analysis, project administration, and visualization. Z.S.: Writing—original draft, conceptualization, investigation, writing—review and editing, methodology, resources, funding acquisition, data curation, validation, supervision, formal analysis, software, project administration, visualization investigation, and writing—review and editing. **Competing interests:** The authors declare that they have no competing interests. **Data and materials availability:** All data needed to evaluate the conclusions in the paper are present in the paper and/or the Supplementary Materials.

Submitted 27 August 2024
Accepted 12 March 2025
Published 18 April 2025
10.1126/sciadv.ads7627